Journal of Petroleum Science and Engineering 196 (2021) 107659

Contents lists available at ScienceDirect

Journal of Petroleum Science and Engineering

journal homepage: http://www.elsevier.com/locate/petrol

Fracture characterization and detection in the deep Cambrian dolostones in the Tarim Basin, China: Insights from borehole image and sonic logs

Jin Lai [a,b,*], Kangjun Chen [b], Yi Xin [b], Xingneng Wu [c], Xu Chen [c], Kefu Yang [c], Qiuqiang Song [c], Guiwen Wang [a,b,**], Xiujian Ding [d]

[a] State Key Laboratory of Petroleum Resources and Prospecting, China University of Petroleum (Beijing), Beijing, 102249, China
[b] College of Geosciences, China University of Petroleum (Beijing), Beijing, 102249, China
[c] Research Institute of Petroleum Exploration and Development, Tarim Oilfield Company, CNPC, Korla, 841000, Xinjiang, China
[d] Key Laboratory of Deep Oil & Gas, China University of Petroleum (East China), Qingdao, 266580, China

ARTICLE INFO

Keywords:
Fractures
In-situ stress
Dolostones
Dissolution
Well log expression
Tarim basin

ABSTRACT

Characterization and detection of natural fractures using well logs in ancient deeply buried dolostones with low matrix porosity are very difficult. Core description, thin section analysis, conventional well logs, borehole image and sonic logs are used to document distribution of fractures in deep Cambrian dolostones in the Tarim Basin, China. The SH_{max} (maximum horizontal stress) direction is determined from drilling induced fractures, borehole breakouts and shear wave birefringence. Natural fractures with various attributes (open to partly open to closed) and orientation (including dip angles) are recognized. Natural fractures are classified into closed fractures, partly closed fractures, vuggy fractures and open fractures, and they can be further classified into high angle fractures, low-medium dip angle fractures, and low angle or horizontal fractures. Natural fractures are mainly associated with the more brittle rocks (dolograinstone, fine-medium-coarse crystalline dolostones), while fractures in dolomicrites and evaporitic gypsums-bearing dolostones are rare.

Open to closed fractures are recognized as dark to bright sine waves on image logs, and the presences of open fractures cause minor deviations on the DEN logs, but significant deviations in resistivity values, while AC will be significantly increased in front of fractures. The energy of sonic full-waveforms will be strongly attenuated in front of open fractures. Fractures with strike parallel to the SH_{max} tend to have large aperture and good connectivity, and are suggested to enhance hydrocarbon productivity. Dolostones adjacent to the deep faults are heavily fractured, and fractures act as the hydrothermal fluid flow pathways, facilitating dissolution process. The abundance of vuggy fractures, and enlargement of the pre-existing microfractures support that fractures had enhanced dissolution. The dissolution along fracture surfaces helps increase fracture porosity. The results of this study about subsurface fracture patterns and their distributions are important for the hydrocarbon exploration and production in the Cambrian dolostones in the Tarim Basin.

1. Introduction

The Cambrian dolostone reservoir is a key hydrocarbon exploration target in the Tarim basin of West China (Zhao et al., 2012; Zhao et al., 2014; Zhu et al., 2015a; Shen et al., 2016; Jiang et al., 2016; Lai et al., 2020). However, the Cambrian dolostones in the Tarim basin have undergone multiple phases of tectonic activity and diagenetic modifications (Jiang et al., 2016, 2018; Lai et al., 2020). Recently abundant hydrocarbons have been produced from the Cambrian dolostone since the first discovery of natural gas in the Well Zs1 in 2012 (Zhao et al., 2012; Li et al., 2016; Dong et al., 2017; Wang et al., 2018; Jiang et al., 2018). The dolostones have been deeply buried (>4000 m) (Li et al., 2016; Jiang et al., 2016), and had experienced multiple phases of tectonic activities (Zhu et al., 2015a; Guo et al., 2018; Tian et al., 2019), resulting in the formation of unconformity, folds, faults, as well as fractures (Su et al., 2016; Lu et al., 2017; Li and Cai, 2017).

Fractures provide hydrocarbon storage spaces and they constitute fluid flow conduits (Nelson, 2001; Zeng, 2010; Xu et al., 2016; Peacock

* Corresponding author. China University of Petroleum (Beijing), 18 Fuxue Road, Changping, Beijing, 102249, China.
** Corresponding author. China University of Petroleum (Beijing), China.
E-mail addresses: sisylaijin@163.com (J. Lai), wanggw@cup.edu.cn (G. Wang).

https://doi.org/10.1016/j.petrol.2020.107659
Received 31 March 2020; Received in revised form 7 July 2020; Accepted 14 July 2020
Available online 17 July 2020

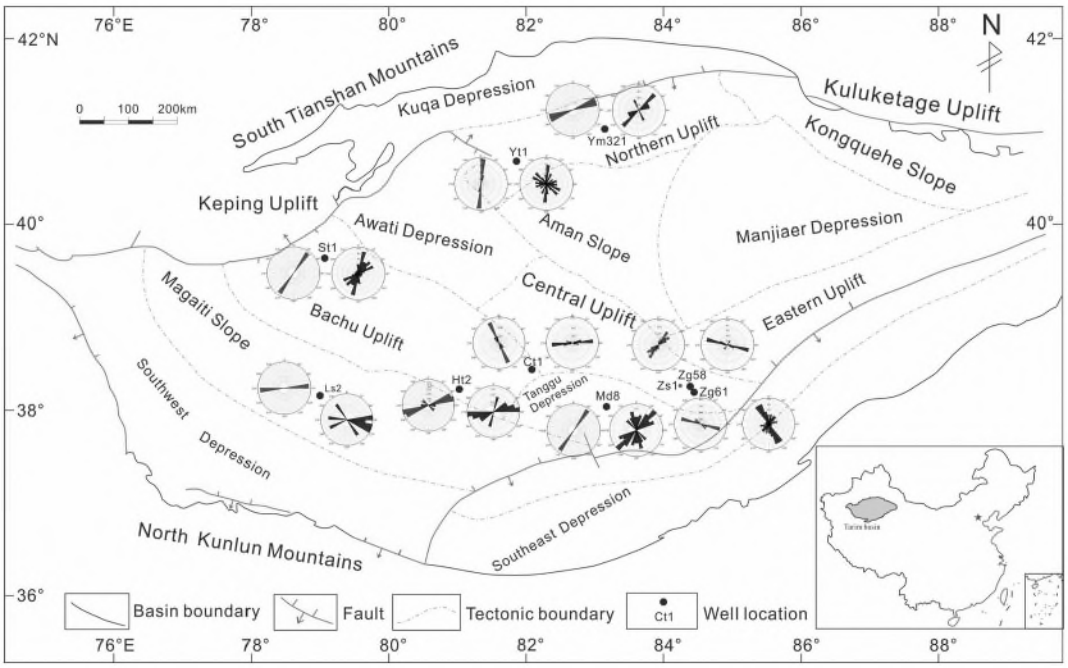

Fig. 1. Structural division map of the Tarim basin within China (Gao and Fan, 2015; Jiang et al., 2016). Note the strike of natural fractures and in-situ stress.

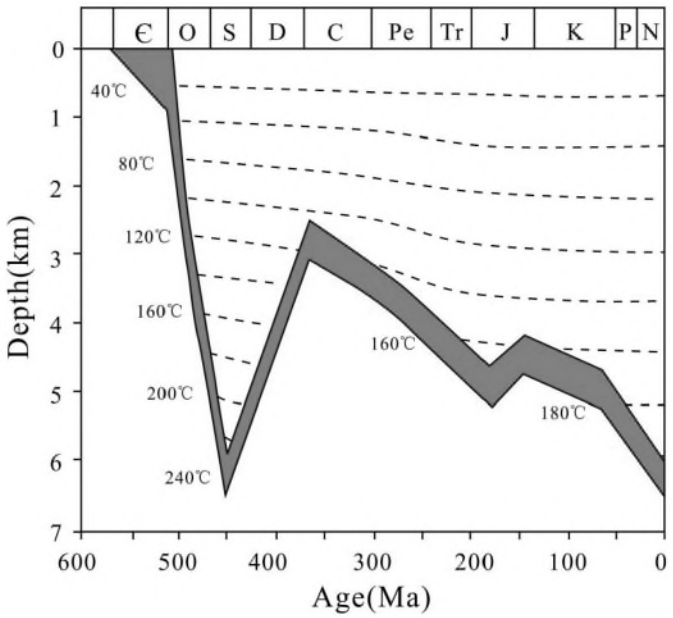

Fig. 2. Burial and geothermal history of the Cambrian (Є) from TZ1 well in Tazhong Uplift (Jiang et al., 2018). C=Carboniferous; D = Devonian; J = Jurassic; K=Cretaceous; N=Neogene; O=Ordovician; P=Paleogene; Pe = Permian; S=Silurian; Tr = Triassic.

et al., 2016). Additionally in carbonate rocks, the faults and fractures are commonly migration conduits for dolomitizing fluids (Warren, 2000; Wilson et al., 2007), and they may act as important flow pathways due to low matrix permeability (Dashti et al., 2018). Fracture-controlled carbonate reservoirs commonly produce more oil than facies-controlled reservoirs (Luczaj et al., 2006), and fractured dolostone reservoirs are one of the most important reservoir types found in the Tarim Basin (Zhu et al., 2015b). However, little is known about the appearance of fracture patterns and well log responses of fractures in the Cambrian dolostones in Tarim basin. Therefore, knowledge of appearance, pattern and distribution of fractures is crucial throughout the lifecycle for hydrocarbon reservoirs (Ameen et al., 2012; Lyu et al., 2016; Dashti et al., 2018). There are direct and indirect methods and data for subsurface fracture detection. Direct core records are highly costly, discontinuous, and they appear as rubble and rock debris in highly fractured zones (Ameen et al., 2012; Dashti et al., 2018), making it difficult to evaluate subsurface fractures (Zeng, 2010). Petrophysical well logs, especially the borehole image and sonic logs provide a continuous clear picture of borehole walls with precise depth and orientation (Khoshbakht et al., 2009; Aghli et al., 2016, 2020; Dashti et al., 2018; Tian et al., 2018). Insights could be provided into the subsurface fractures through a comprehensive use of cores, borehole image logs, and full-wave sonic logs.

Therefore, from both scientific and practical standpoints, it is of great importance to describe the fractures and correlate them with well logs with the aim to detect subsurface fractures. The main goal of this study is to address the following three issues:

1) The appearances of fractures in various lithology of the deeply buried dolostones with very low matrix porosity, and their responses on the image and sonic logs.
2) The relationship between in-situ stress direction and fracture parameter.
3) The impact of fractures in improving reservoir quality by enhancing dissolution.

2. Geological setting

The petroliferous Tarim Basin is located between the Tianshan and Kunlun Mountains with an area of 56 × 10^4 km^2 (Fig. 1) (Qiu et al., 2012; Gao et al., 2016; Lai et al., 2017a; Fu, 2019). The Tarim basin had experienced multiple stages of tectonic evolution including Caledonian (Early Ordovician to Late Silurian), Hercynian (Middle Devonian to Early Permian), Indosinian (Late Triassic), and Himalayan (Neogene) orogenic movements (Zhang et al., 2009; Dong et al., 2013; Zhu et al., 2015a; Guo et al., 2018; Ngia et al., 2019). The multiple evolutionary stages results in the today's tectonic configuration of the Tarim Basin (three major uplifts and four depressions) (Fig. 1) (Du et al., 2018), and many deep faults and fractures were formed during the multistage tectonic influences (Zhu et al., 2015a). The active faults and fractures communicate with the source rocks and the overlying Cambrian

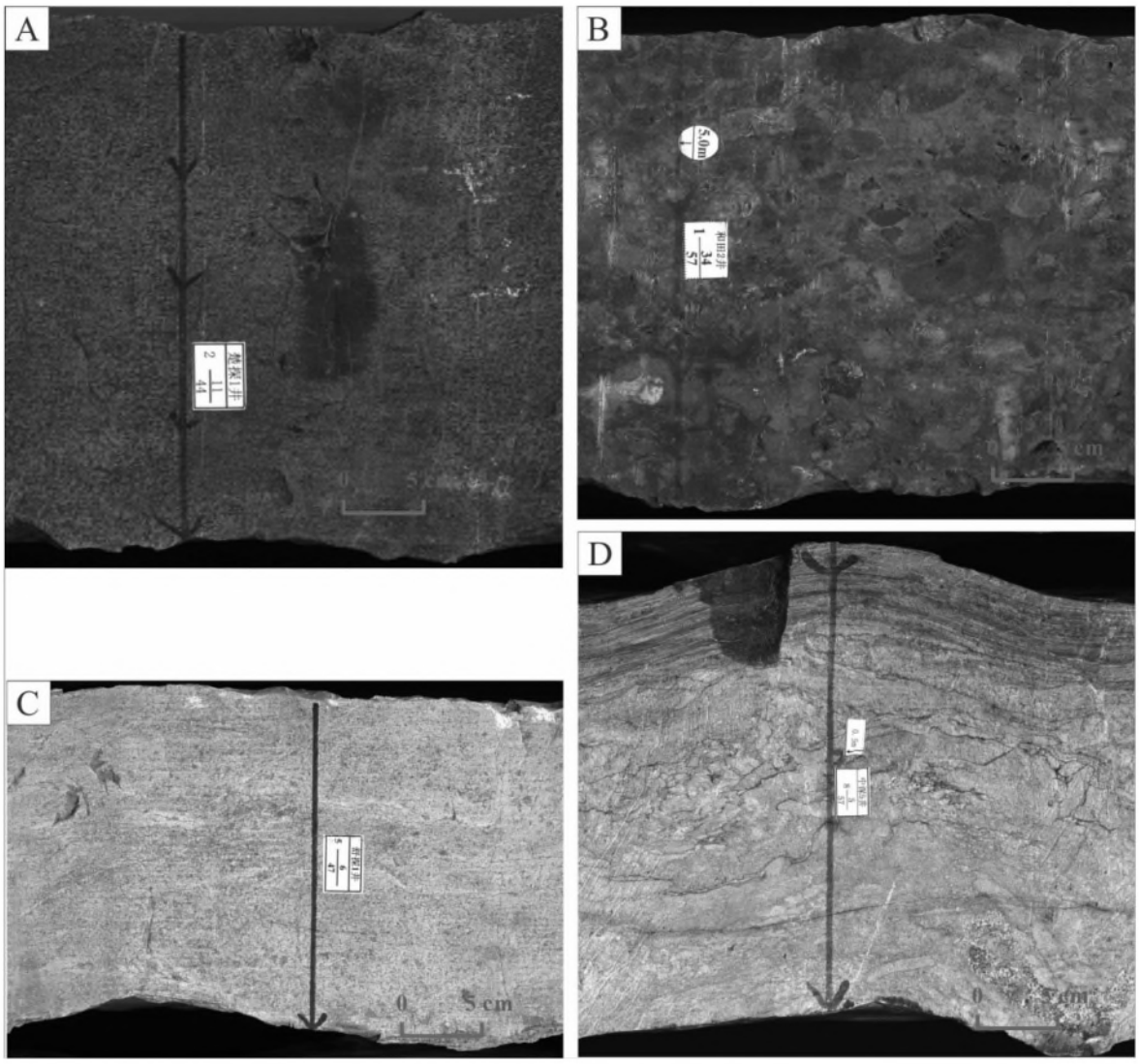

A. Dolomicrites, Ct1, 7765.76m

B. Grain (residual) dolostones, Ht2

C. Medium-coarse crystalline dolostones, St1

D. Gypsum beds and nodules, Zs5

Fig. 3. Core photos of lithology of Cambrian dolostones in Tarim Basin.

dolostone reservoirs act as the hydrocarbon migration pathways (Jiang et al., 2015). In addition, abundant pores, and vugs were formed due to dolomitization processes and other diagenetic modifications (Zhu et al., 2015a; Jiang et al., 2016), resulting in the formation of high quality reservoirs in the deeply buried Cambrian dolostones (Jiang et al., 2018).

The thickness of Sinian to Quaternary sedimentary rock in the Tarim Basin is up to 15, 000 m (Chen et al., 2000). From the late Neoproterozoic to late Ordovician, a shallow carbonate platform (interior, margin, slope and basin depositional facies) was developed in the Tarim Basin, and thick carbonate successions (up to 2000 m) were deposited (Dong et al., 2013; Du et al., 2018; Fu, 2019; Hu et al., 2019). The carbonate deposition was terminated at the end of late Ordovician (Dong et al., 2013; Du et al., 2018). The Cambrian and Lower Ordovician (Penglaiba Formation) in the Tarim Basin are now composed of dolostone successions (Gao and Fan, 2015). The Cambrian can be divided into 6 Formations including Yuertusi ($\epsilon_1 y$), Xiaoerbulake ($\epsilon_1 x$), Wusonggeer ($\epsilon_1 w$), Shayilike ($\epsilon_2 s$), Awatage ($\epsilon_2 a$) and Qiulitage ($\epsilon_3 q$) Formation (Gao and Fan, 2015; Jiang et al., 2018). The Lower Cambrian is composed mainly of dolostones, while the Middle Cambrian consists of a set of evaporite-bearing sequences, and the Upper Cambrian is composed of thick dolostones (Zhang et al., 2009). The burial and geothermal history reconstruction was based on the work Jiang et al. (2018). The Cambrian strata had been rapidly buried to a depth of 5000–8000 m during late Ordovician, and reached a maximum temperature of >200 °C, and then was eroded 2000 and 3500 m thickness strata due to regional uplift (Fig. 2) (Jiang et al., 2018). Intense volcanic activity took place extensively in Tarim block during the Permian time (Dong et al., 2013).

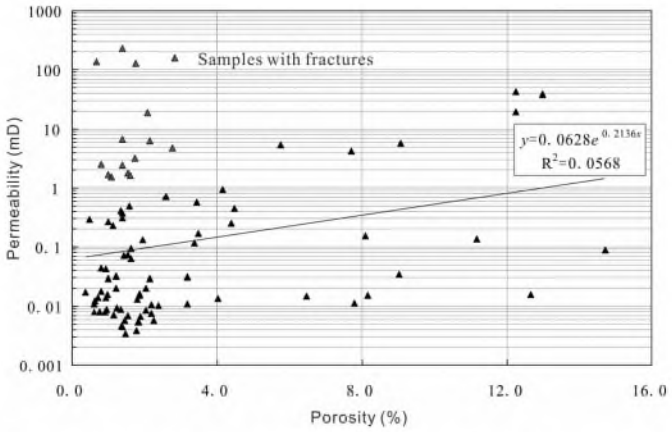

Fig. 4. Crossplot of permeability versus porosity of Cambrian dolostones in Tarim Basin. Note the samples with fractures (low porosity but high permeability).

The Early Cambrian Xiaoerbulake in Tarim Basin is dominated by carbonate slope facies, and grain bank, algal mounds are widely developed. The Lower to Middle Cambrian Wusonggeer, Awatage Formation, which are gypsum bearing dolostone sequences, were deposited in a evaporative carbonate platform, and restricted lagoonal (evaporated lagoon) and tidal-flat (evaporitic flat) facies are widely developed (Jiang et al., 2018). The Middle Cambrian Shayilike Formation is characterized by intra-platform shoal and bank facies (Jiang et al., 2018). The Upper Cambrian Xiaqiulitage Formation is deposited in large shallow restricted platform, and the depositional micro-facies includes reef-shoal (platform margin and intra-platform) mico-facies, interbank sea (Du et al., 2018).

3. Data and methods

Macroscopic fracture observations are based on about 160 m length of cores. Cores were taken from 10 wells recently drilled in the Tarim basin in water based drilling muds, and were cut into core plugs with diameters of 2.5 cm and lengths ranging from 2.5 to 5.0 cm. Representative core plugs (fractured-vuggy dolostones, finely to medium crystalline dolostones, dolomicrites) were selected for thin section petrological analysis (optical transmitted light and CL microscopy) in order to detect the pore systems and particularly micro-fractures (with aperture<0.1 mm) (Anders et al., 2014). Blue fluorescent epoxy was impregnated to help identify pores and micro-fractures, and the thin sections were stained with mixed Alizarin Red S and potassium ferricyanide solution to help recognize the different minerals.

The whole suite of conventional well logs run in the wells included caliper (CAL), natural gamma ray (GR), litho-density (Pe), and high-definition resistivity logs (M2R2, M2R3, …, M2Rx). The three porosity logs include the sonic transit time (AC), compensated neutron porosity (CNL), and bulk density (DEN). The core-log depth matching was made by correlating core-measured gamma ray/density with GR log or bulk density log to identify distinctive features (Lai et al., 2017b).

The Schlumberger's FMI (Fullbore Formation MicroImager) and Haliborton's XRMI (Extended Range Micro Imager) imaging tool was used to get high-resolution "pseudo-picture" of borehole walls. The borehole coverage of FMI and XRMI in an 8.0-inch borehole is 80% and 60%, respectively, and the vertical resolution is 5 mm (Lai et al., 2018). A total of 8 pads were fixed on the FMI imaging tool, and each pad contains 24 buttons, therefore 192 micro-resistivity curves can be collected during FMI logging (Khoshbakht et al., 2009; Lai et al., 2017c; Nian et al., 2018). For XRMI, the pad is 6, and the buttons fixed on each pad is 25 (Wang et al., 2020; Lai et al., 2018). Then the numerical matrix of the raw measured resistivity can be converted to colorful images, i.e., "pseudo-picture" of borehole walls, through basic pre-processing workflows including speed correction, eccentering correction, and normalization (Schlumberger, 2004; Khoshbakht et al., 2009; Folkestad et al., 2012; Nian et al., 2017; Lai et al., 2018; Lai et al., 2019b). The cylindrical image is presented from left to right along the direction north–east–south–west–north (0–360°) (Nie et al., 2013; Lai et al., 2017d). The Pad 1, which can be used for azimuth correction, is shown as the vertical green line (Brekke et al., 2017), while the eight broad white bands refer to the eight pads. Then the fractures (natural and induced) can be picked out from the image logs by fitting sine waves (Goodall et al., 1998; Nian et al., 2016; Keeton et al., 2015; Lai et al., 2019a). Additionally, the dip direction and dip angles of fractures can be derived from the manually traced sine waves (Goodall et al., 1998; Keeton et al., 2015).

XMAC log is one type of cross-dipole array sonic log developed by Baker Hughes Company (the other two are Halliburton's WaveSonic tool, Schlumberger's dipole sonic imager) (Liu et al., 2018). XMAC log records full wave-forms (amplitudes), and the compressional wave slownesses, shear-wave slownesses, Vp/Vs ratio, Stoneley wave and pseudo- Rayleigh waves can be extracted (Crampin, 1985; Collett et al., 2011; Liu et al., 2018). XMAC log is widely used for determining in situ stress fields and anisotropy of rocks by shear wave birefringence, and the direction of the fast shear wave indicates the SH_{max} (present-day maximum horizontal compressive stress) orientation (Liu et al., 2017, 2018; Zhao et al., 2018).

4. Results

4.1. Lithology and reservoir quality

The Cambrian strata in Tarim Basin are dominantly dolomicrites (Fig. 3A), dolograinstones (residual ooid grains, intraclasts) (Fig. 3B), and fine-medium-coarse crystalline dolostones (Fig. 3C) (Jiang et al., 2016; Ngia et al., 2019; Lai et al., 2020). The gypsums and salt occur as nodules or beds within the Cambrian dolostones (Fig. 3D) (Ngia et al., 2019). The microbial dolomites (algal-laminated) are also found in the Keping-Bachu Uplift of Tarim basin (Wang et al., 2018; Ngia et al., 2019). In the Cambrian dolostones of Tarim Basin, the dolomicrites or very fine crystalline dolomites are dark grey to brown grey in color, while the fine to medium-to-coarse crystalline dolomites are white, pale brown, and light grey (Fig. 3) (Zhu et al., 2015a; Lai et al., 2020).

Reservoir quality in dolostones is the comprehensive reflection of depositional facies, diagenesis, and fractures (Lai et al., 2019c; Jafari et al., 2020). The reservoir quality of the Cambiran dolostones is poor according to routine core analysis (core plugs), and the porosity is in the narrow range from 1.0% to 10.0% (Fig. 4). Therefore the presences of fractures play an important role in enhancing permeability, and it can be concluded from Fig. 4 that permeability can san four order of magnitudes at a certain porosity value.

4.2. In-situ stress direction

In-situ stress status determines the fracture openness and connectivity. Hydrocarbon production rate is highly related to fracture density and their connectivity, therefore in situ stress state determination and natural fracture characterization are important for drilling engineering, hydraulic stimulation and hydrocarbon production (Nelson, 2001; Olson et al., 2009; Zeng and Li, 2009; Lynn, 2016; Nian et al., 2016; Ju et al., 2017; Niu et al., 2020).

4.2.1. Induced fractures and borehole breakouts

Drilling-induced fractures are generated at the time of drilling (Brudy and Zoback, 1999; Dashti et al., 2018). Both the drilling induced fractures and borehole breakouts from image logs can give the direction of SH_{max} (Wilson et al., 2015; Lai et al., 2018). Induced fractures and borehole breakouts, are easily recognized on images and to be differentiated from natural fractures, as they appear at two symmetrical

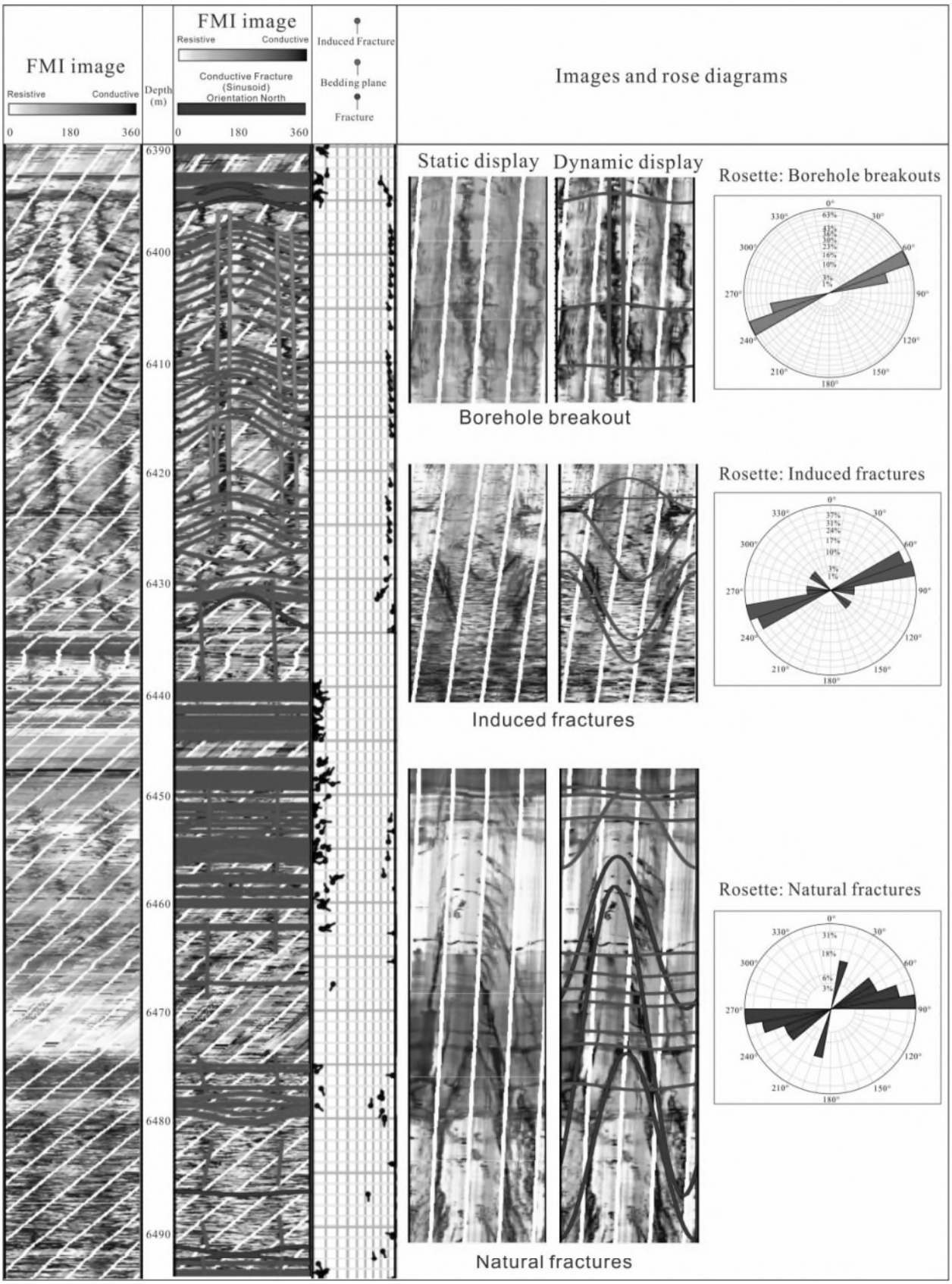

Fig. 5. Comprehensive image log-derived map of natural fractures, induced fractures and borehole breakouts in Well Ht2. Note that the strike of natural fracture are mostly parallel to the induced fractures.

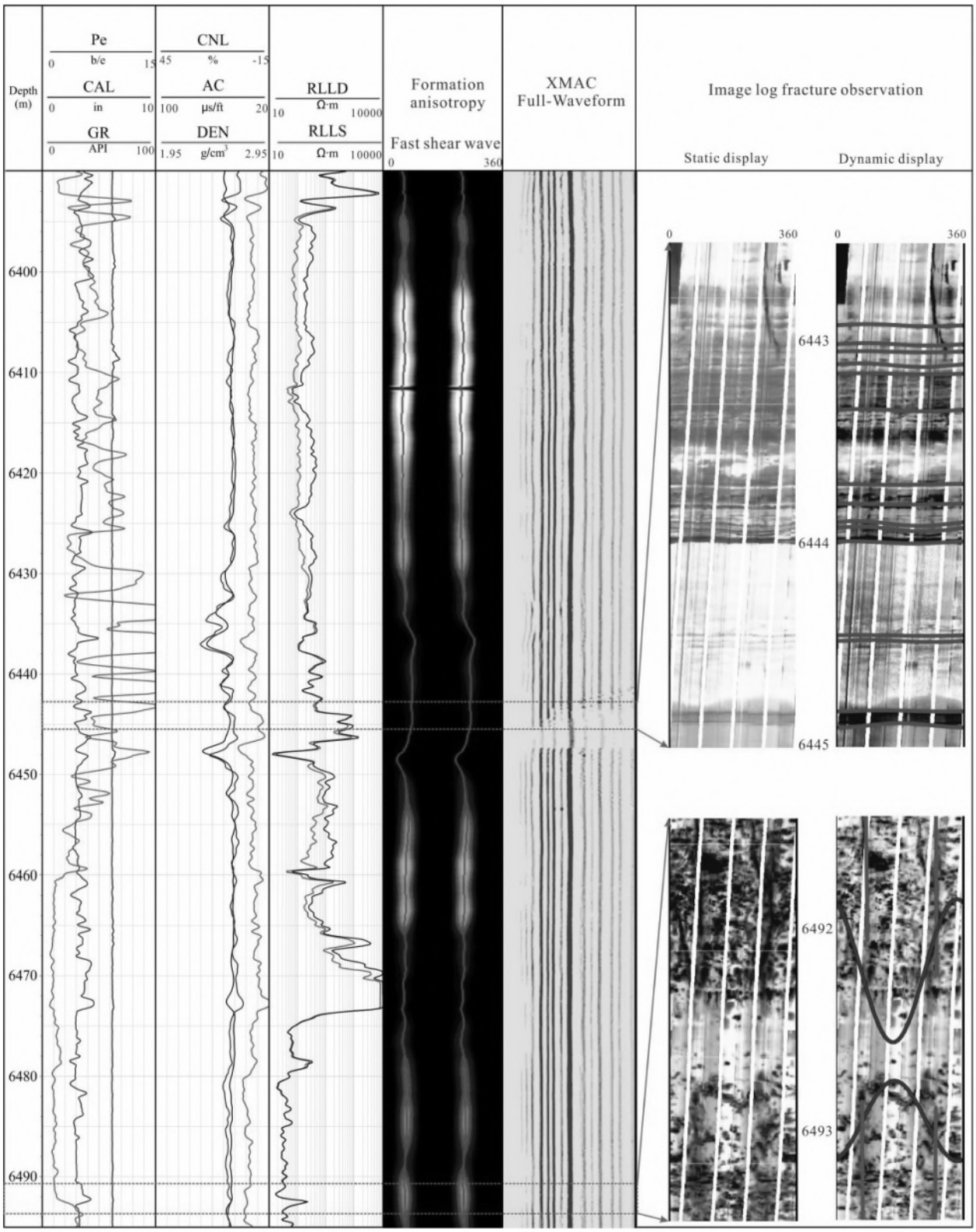

Fig. 6. Comprehensive map of XMAC full-waveform sonic, fast shear wave orientation and related image logs in Well Ht 2. The presence of natural fracture will cause attenuation of full-waveform sonic.

azimuths (Etchecopar et al., 2013). Borehole breakouts are wellbore enlargements formed due to compressive failure, and they indicate the horizontal minimum stress orientation (Sh_{min}) (Bell and Gough, 1979; Nian et al., 2016). The borehole breakouts of Well Ht2 occur as vertical broad dark bands, and give a SH_{max} orientation of 60–80° (Fig. 5). There are two types of drilling induced (open mode) fractures, including (1) "two-way" type (two nearly vertical fracture oriented at 180° from each other), and (2) en-echelon type (traced 180° offset at the borehole wall and have en-echelon arrangement) (Brudy and Zoback, 1999; Prioul et al., 2007; Ameen et al., 2012; Nian et al., 2016; Lai et al., 2019a). The

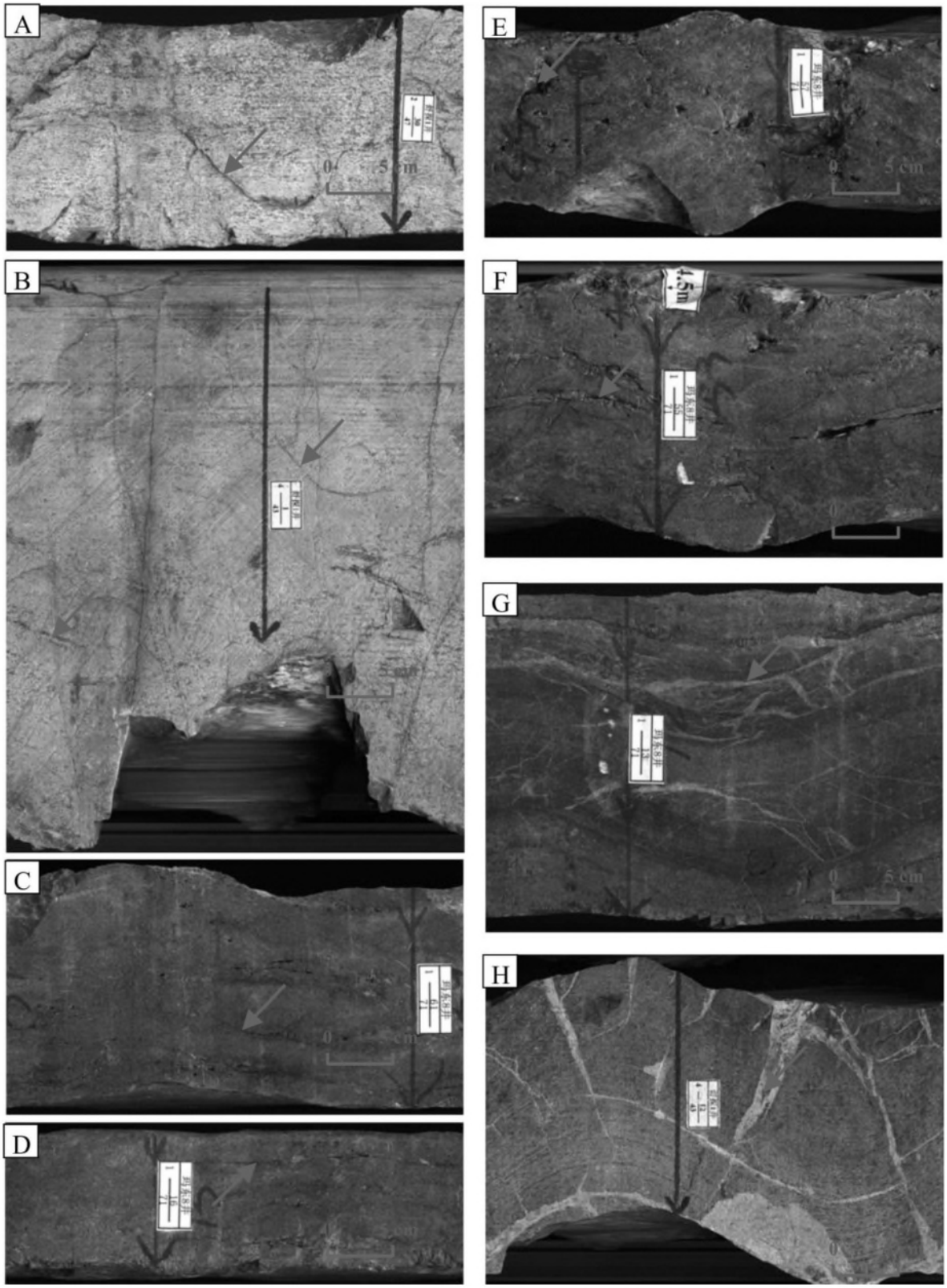

Fig. 7. Core photos showing the fractures of various attributes (low to high dip angles) and status (open, sealed and closed) of dolostones in Tarim Basin. A. High-angle open fractures, St1; B. Composite open fractures of high and low angle, St1; C. Low angle fractures, Md8; D. Low angle fracture, Md8; E. Dissolution along fracture plane, Md8; F. Partly filled log angle fractures, Md8; G. Closed low angle fractures, Md8; H. Closed high angle fractures, St1.

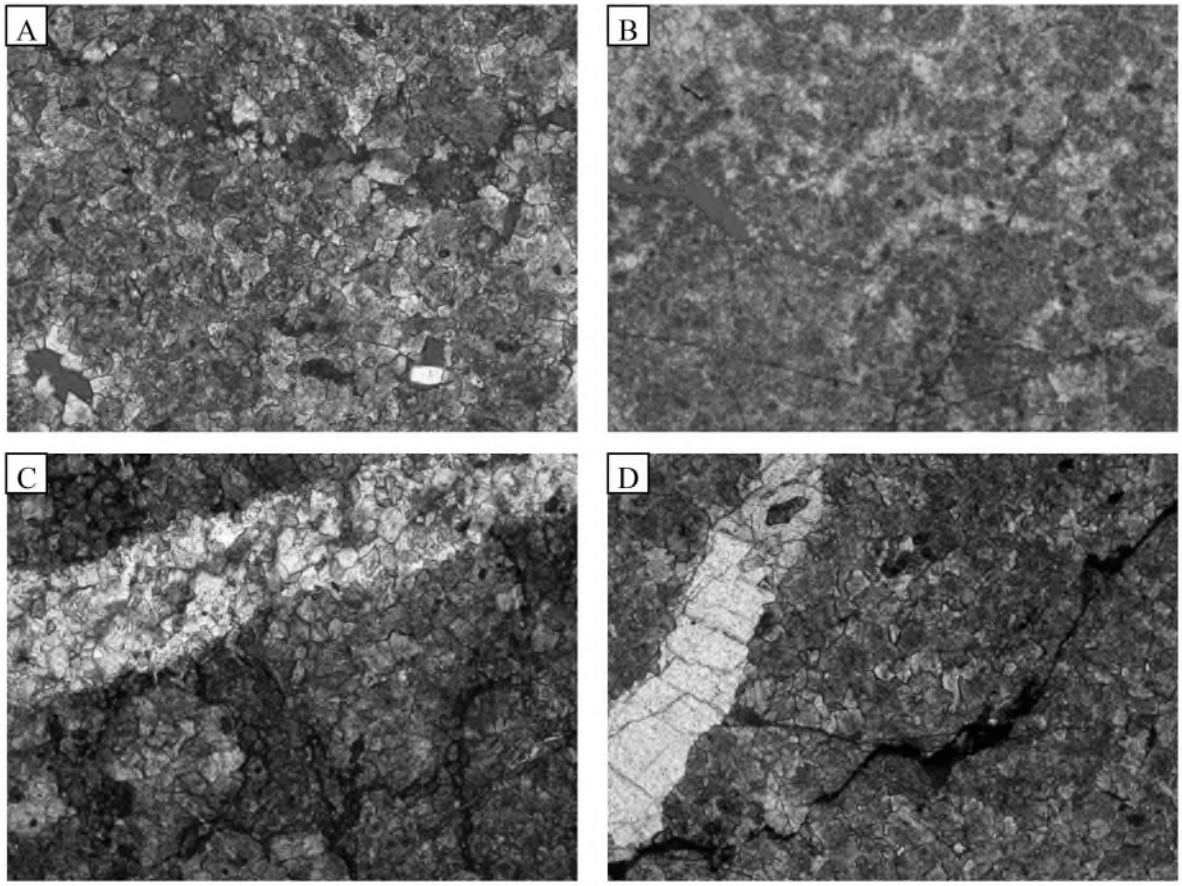

Fig. 8. Thin sections showing the microfractures of the Cambrian dolostones in Tarim Basin. A. Dissolution along the fracture planes, Ct1, 7769.64 m. B. Well developed microfracture network, Zg582, 3626.02 m. C. Gypsum filling the microfractures, Ct1, 7764.99 m. D. Bitumen filling the microfractures, Ct1, 7764.9 m.

high angle en-echelon type induced fractures in Fig. 5 indicate a dominant SH_{max} orientation of 60–80°, which is in consistent with the SH_{max} direction determined from borehole breakouts (Fig. 5).

4.2.2. Shear wave birefringence

The formation anisotropy will result in variations of shear wave velocities and further varied polarization orientations of shear waves (Liu et al., 2018). Therefore XMAC (cross-dipole) borehole acoustic log is an effective method for stress field determination according to the shear wave birefringence, and the direction of the fast shear wave gives the orientation of SH_{max} (Liu et al., 2017). The XMAC anisotropy analysis results show that the direction of SH_{max} is 60–70° in the 6390–6495 m depth intervals (Fig. 6). It is observed that the SH_{max} direction given by image logs in Fig. 5 is in line with the fast shear wave direction (Fig. 6). However, it should be noted that in intervals with fractures (6435–6450 m) (Fig. 5), the offset of fast shear wave is observed, and the direction of shear waves is located at about 80–90° (Fig. 6). Abundant cross bedding (green sine waves) with low dip angles are recognized in this interval from image-log based fracture observation (Figss. 5–6).

4.3. Fracture characteristics

Natural fractures refer to discontinuities caused by brittle and semi-brittle deformation of rocks (Nelson, 2001, Peacock, 2001; Brandes and Tanner, 2020). Core observations reveal that there are abundant fractures with various attributes (dip angles) and status (open to partly open to closed) in the Cambrian dolostones of the Tarim Basin (Fig. 7). High angle fractures, which tend to have larger fracture aperture, could still remain open status at a great depth >5000 m (Fig. 7A) (Lai et al., 2018). In addition, they can constitute a well-developed fracture networks together with the low angle fractures (Fig. 7B). The low angle or horizontal fractures are suggested to have lower aperture that those high angle fractures (Fig. 7C and D). Dissolution along the fracture planes are commonly observed, which implies that the fractures occurred before dissolution, forming vuggy fractures (Zhu et al., 2015b) (Fig. 7E). The vuggy fractures refer to the fractures enhanced by dissolution later during the diagenetic history (Dashti et al., 2018).

From Fig. 7 it can be concluded that the natural fractures are mainly associated with the brittle rocks (dolograinstone, fine-medium-coarse crystalline dolostones) (white or grey), while fractures in the basinal or interbank dolomicrites and evaporitic gypsums-bearing dolostones are rare.

Additionally microfractures with various apertures are commonly observed by thin sections (Fig. 8). Actually most of the microfractures (<0.1 mm), which are detected by thin section petrography, are observed to have enhanced dissolution (Fig. 8A and B), and the various microfractures could constitute a well developed microfracture network (Fig. 8B). However, some of the early formed fractures, are partly or fully filled with calcite, dolomite and quartz cements, forming partly closed or sealed fractures (Fig. 7F–H). The thin section analysis proves the presences of microfractures filled with various types of cements (Fig. 8C and D). Noting that fractures are also important migration pathways for hydrothermal fluids, and the hydrothermal fluids will dolomitize the precursor limestones, forming saddle dolomites and hydrothermal dolostone reservoirs (Zhang et al., 2009; Zhao et al., 2012; Jiang et al., 2016).

Thin section observation also support that microfractures are mainly associated with the dolograinstone (Fig. 8A and B) and fine-medium-coarse crystalline dolostones (Fig. 8C and D).

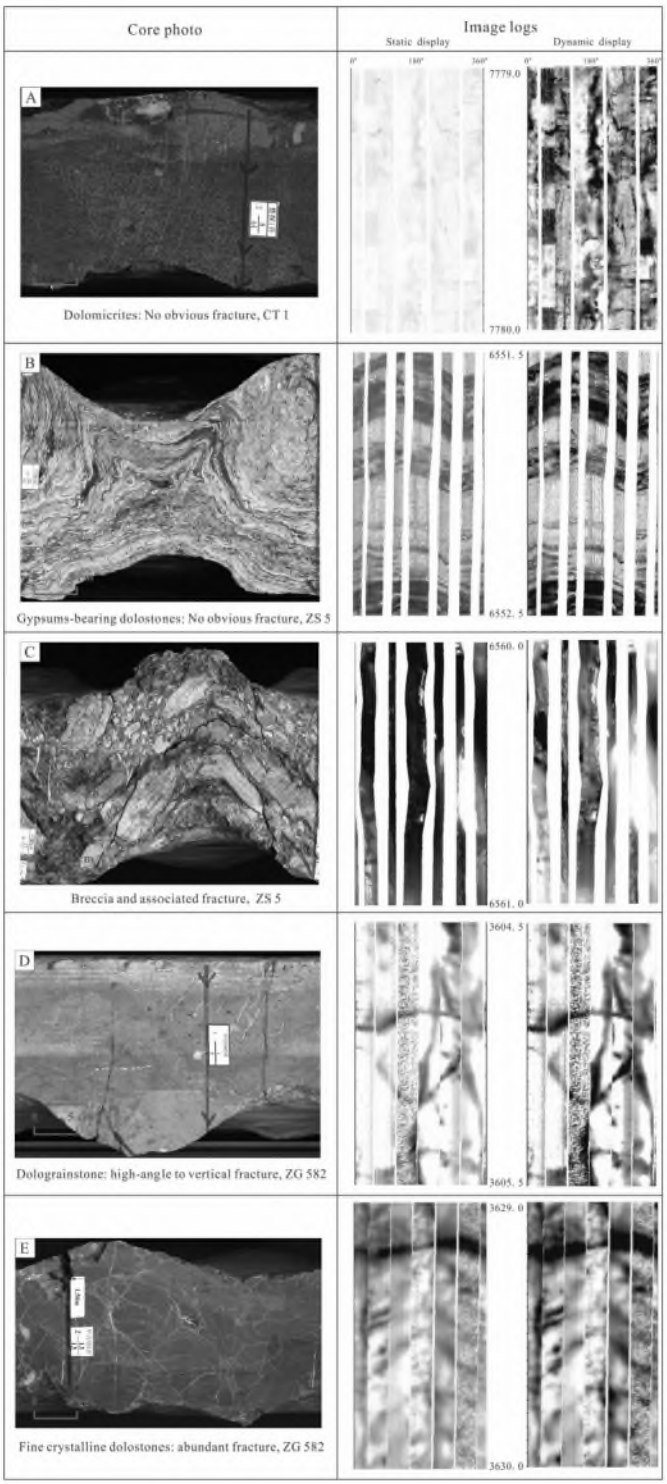

Fig. 9. Appearances of natural fractures in various lithology of the Cambrian dolostones in Tarim Basin. Natural fractures are mainly associated with the brittle rocks (dolograinstone, fine-medium-coarse crystalline dolostones), while the basinal or interbank dolomicrites and evaporitic gypsums-bearing dolostones are difficult to be fractured.

4.4. Well log expressions of natural fractures

In terms of facilitating well log interpretation in this study, the natural fractures in the Cambrian dolostones of Tarim Basin are classified as closed fractures, partly closed fractures, vuggy fractures and open fractures. Additionally the open fractures are further classified into high angle fractures (>60° dip angle), low-medium dip angle fractures (30–60°), and low angle or horizontal fractures (<30°).

By calibrating core with image logs (Fig. 9), it's confirmed that there are no evident fracture appearances in the dolomicrites (dark grey) and gypsums-bearing dolostones (Fig. 9A and B). The image log fracture observation is in accordance with the core. Additionally, it should be noted there are many bedding planes within the gypsums-bearing dolostones, which are easily to be detected on image logs. These beddings look like very like bedding fractures by image logs, however, though are easily to be picked out as sine waves, they are not natural fractures since the bedding fractures are parallel to the layer surfaces (Fig. 9B). However, breccia and associated fracture porosity can be observed in anhydrite-bearing sections if the anhydrite/gypsum occurs as breccias (Fig. 9C) (Jiang et al., 2018). Conversely, abundant natural fractures are associated with the dolograinstone, and fine-medium-coarse crystalline dolostones (white or grey in color), and the related image logs (large amounts of dark sine waves) supports this finding (Fig. 9D and E).

Direct core fracture observations are correlated with well logs to indirectly express the various types of natural fractures using well logs. Many conventional log curves will show deviations from the normal conditions in front of fractures, especially the presence of open fractures (Shazly and Tarabees, 2013). The presences of fractures will cause minor deviations on the CAL, GR and DEN logs, and sonic interval transit time (AC) will be significantly increased in front of fractures (especially low angle and horizontal fractures) (Fig. 10) (Jafari et al., 2012; Zazoun, 2013). High dip angle fractures will result in a positive deviation on the dual lateral log (RLLD > RLLS) (Shazly and Tarabees, 2013). The presence of horizontal or low angle fractures will contribute to a rapid decrease in RLLD and therefore RLLS is higher than RLLD (negative deviation of dual lateral log) (Shazly and Tarabees, 2013).

The high angle open fractures in the 3607–3608 m depth intervals have caused a minor deviation on the bulk density, while the AC value is highly increased (Fig. 10). Core observation proves that there are two high angle fractures, and open dissolution vugs are also detected (Fig. 10). Both the high angle fractures and network fractures result in a significant decrease in resistivity values, and the presences of network fracture systems (composite fractures with horizontal, low angle and high angle fractures) (3626.5–3627.5 m) cause an evident positive deviations, and there are no obvious deviations of dual lateral log in the high angle fracture intervals (Fig. 10). Core observations support that dissolution along the fracture planes have occurred, and vugs are observed coexisting with the fracture network (Fig. 10).

For the partly closed to closed fracture systems, it has been recognized that there are no evident deviations on all of the conventional logs. For instance, the presences of closed fractures, which are filled by calcite cements according to the core observation, are difficult to be identified on the conventional logs. The closed fracture and partly closed fractures have not caused evident deviations in bulk density and sonic transit time compared with the normal well log responses, and only the resistivity values are slightly decreased (Fig. 11).

Consequently, the prediction of partly to fully closed fractures via conventional well logs remains a challenging task. Additionally open factures with various attributes have varied responses on the conventional well logs, making it difficult to determine the fracture status and connectivity using conventional well logs alone. Actually, neither of these well log response patterns above can be taken as a conclusive evidence of open fractures because other factors such as lithology, borehole environments and fluid property, and a combination of conventional logs should be used for fracture detection (Zazoun, 2013; Aleardi et al., 2015; Lai et al., 2017b; Aghli et al., 2016). In addition, image and array sonic logs, which are treated as advanced well logging techniques, should be introduced to predict the subsurface fractures.

Natural fractures are evidently recognized on the electrical image logs collected in water-based drilling muds (Fig. 10) (Ameen et al., 2012). Natural open fracture planes will appear as dark continuous

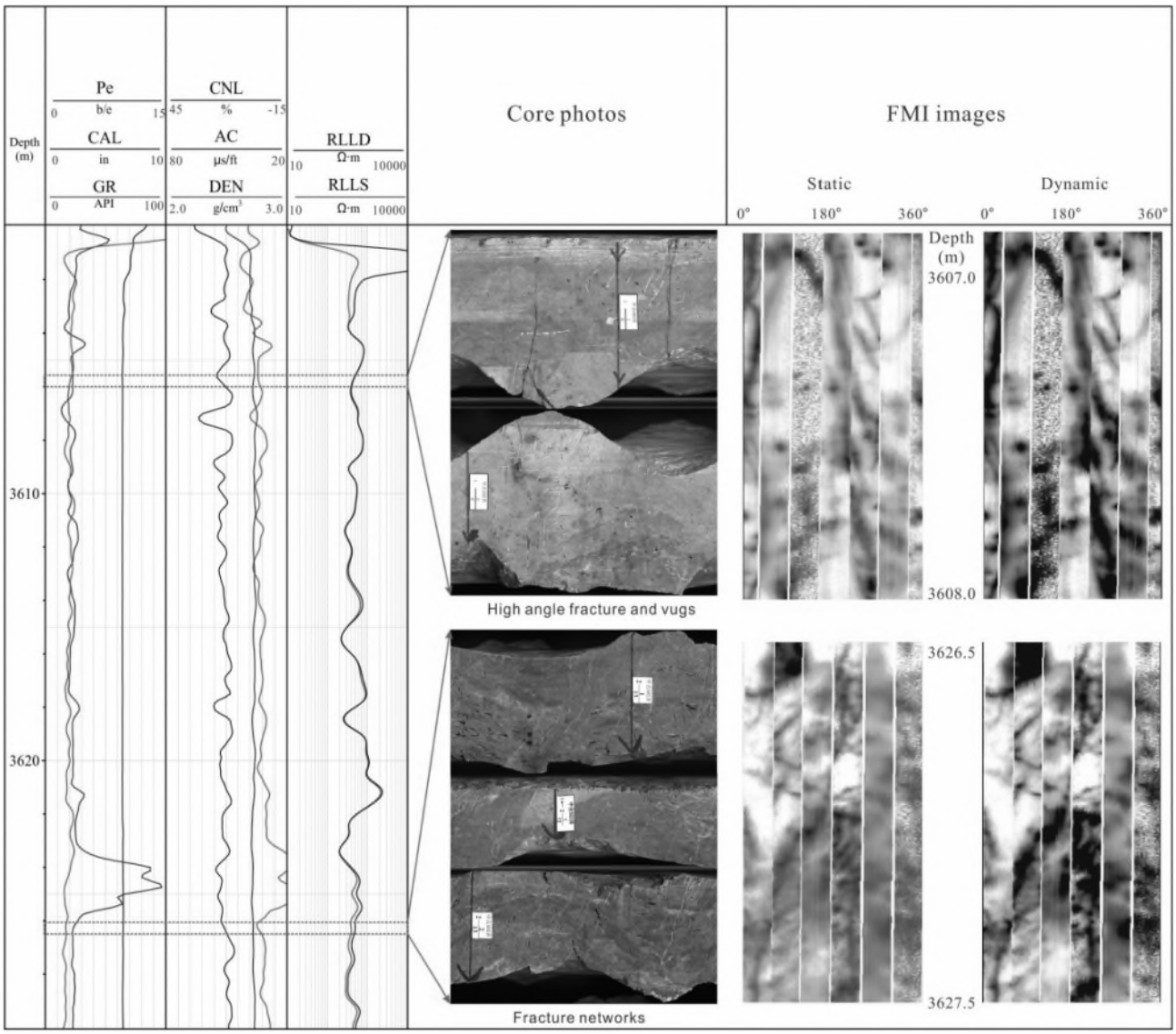

Fig. 10. Well log expressions of open high angle fractures and fracture network in the Cambrian dolostones in Tarim Basin (Zg582). Natural fractures are recognized as dark sine waves on image logs.

sinusoidal waves on the unrolled images (Khoshbakht et al., 2009), and the amplitude indicates the dip angle, and the lowest point is the dip direction (Fig. 10) (Goodall et al., 1998; Keeton et al., 2015). During well drilling, the conductive drilling muds (water based muds) will fill the natural open fractures, and therefore have low resistivity compared with the normal rocks (Dashti et al., 2018). The fracture planes are intersecting with the depositional beds (bed boundary or cross beddings). The partially closed to closed fractures are recognized as bright discontinuous sinusoidal waves (Fig. 11). Therefore the image logs can be used for the determination of fracture orientation (strike and dip), fracture attributes (dip angles) and fracture status (open or closed) (Goodall et al., 1998; Lai et al., 2018). Natural fractures can be differentiated with drilling-induced fractures because they have planar appearances and can be picked as sinusoids, while the drilling induced fractures appear as non-planar or nearly vertical, and they were picked as two linear traces (magenta colors) on opposite sides of the borehole wall (180° apart in the unrolled images) (Fig. 5) (Dashti et al., 2018).

The array sonic logs are also widely used for fracture detection, and the presences of fractures will decrease the sonic wave velocities and therefore wave impedances (Prioul et al., 2007), therefore sonic full-waveform will be significantly attenuated in cases of open fractures (Assousa and Elkington, 2014; Zaree et al., 2016). In the 5996 m–6000 m depth intervals, the full-waveform of XMAC array acoustic logs are strongly attenuated, forming "V" shape interferometric fringes (Fig. 12). The increase of sonic transit time, decrease of resistivity and the dark sine waves on the image logs prove the existences of fractures in the three depth intervals (5996–6000 m, 6015–6017 m, and 6034–6036 m), and the energy of XMAC full-waveforms are all strongly attenuated in the three fracture zones (Fig. 12).

5. Discussion

5.1. Natural fractures within in situ stress fields

The in situ stress orientation determined from image logs or XMAC sonic logs, as well as the direction (strike) of natural fractures picked out from image logs of all the 9 wells are presented in Fig. 1. The strike composite rose diagram concluded that natural fracture strike of almost all the wells are oriented parallel to the SH_{max} orientation (Fig. 1). Most of the natural fractures have high dip angle (>60°) with two dominant strike directions towards NE-SW. The natural fractures in Wells Ht 2 and Ls 2 have nearly W-E strike (Fig. 1). Image log fracture observations

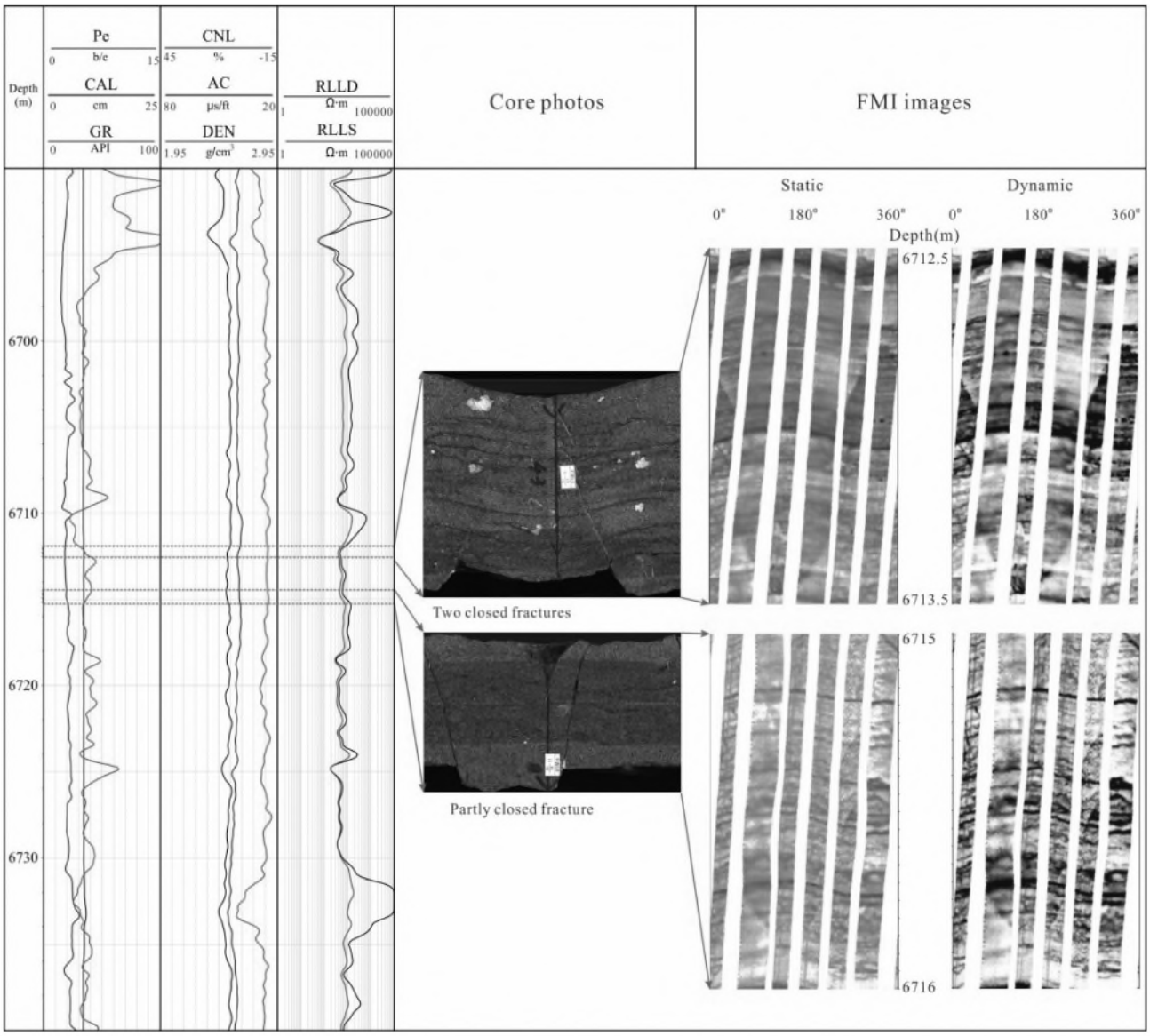

Fig. 11. Well log expressions of partly closed to closed fractures in the Cambrian dolostones in Tarim Basin (Zs5). Partly closed to closed fractures are recognized as dark-bright discontinuous sine waves.

reveal that the main orientation of natural fractures (strike of 60–90°) obtained in Well Ht2 is in good accordance with SH_{max} direction (strike of 60–90°) determined from induced fractures and borehole breakouts (Fig. 5). However, for the Wells Zg58, Zg61 in the Central uplift (Tazhong uplift) and Well Ct1 in the Bachu Uplift, the strike of the natural fractures are not in accordance with SH_{max} direction (Fig. 1). Natural fractures are suggested to have large aperture and good connectivity when they are oriented parallel or within 30° intersection angle to SH_{max} direction (Zeng and Li, 2009; Lai et al., 2017b). Conversely fractures perpendicular to current maximum horizontal compressive stress tend to have a poor connectivity and low aperture (Lai et al., 2018).

The natural fractures picked out from image logs in Well YM321, are observed to be parallel to SH_{max} direction (Fig. 1). The natural fractures on the image logs, which appear as dark sinusoidal waves, have large apertures and good connectivity, and the presences of fractures enhance the hydrocarbon productivity significantly (Fig. 13). As can be observed from Fig. 13, for the intervals ranging from 5335.55 to 5351.27 m, high oil production rate (a daily oil production of 127.08 m^3) is encountered at a drawdown pressure of 9.0 MPa and a choke width of 5 mm (Fig. 13). Conversely, the fracture numbers in Well Ct 1 are low, and natural fractures are not aligned to direction of SH_{max} (Fig. 13). The oil test data reveal that only water is produced from the intervals 7740.0–7782.0 m in Well Ct1. Therefore the presences of fractures, especially those fractures parallel to SH_{max} orientation, play an important role in enhancing oil productivity (Fig. 13).

5.2. Fracture enhanced dissolution

The effect of fracturing on enhancing dissolution, which can be evidenced by vuggy fractures, has been documented by many authors (Zazoun, 2013; Lai et al., 2018; Dashti et al., 2018). The effects of fracturing on reservoir quality in dolostones depended on relative timing of fracturing versus dolomitization processes, dissolution and cementation along fracture planes (Wilson et al., 2007). In dolostones, the late-stage dolomitization postdating fracture formation, and the cementation will reduce reservoir quality in fractured dolostone reservoirs (Wilson et al., 2007). In the Cambrian dolostones in Tarim basin, most of the open fractures have been slightly enhanced by later dissolution, maybe in part related to meteoric diagenesis and burial dissolution (Jiang et al., 2016), and core observation and image log fracture

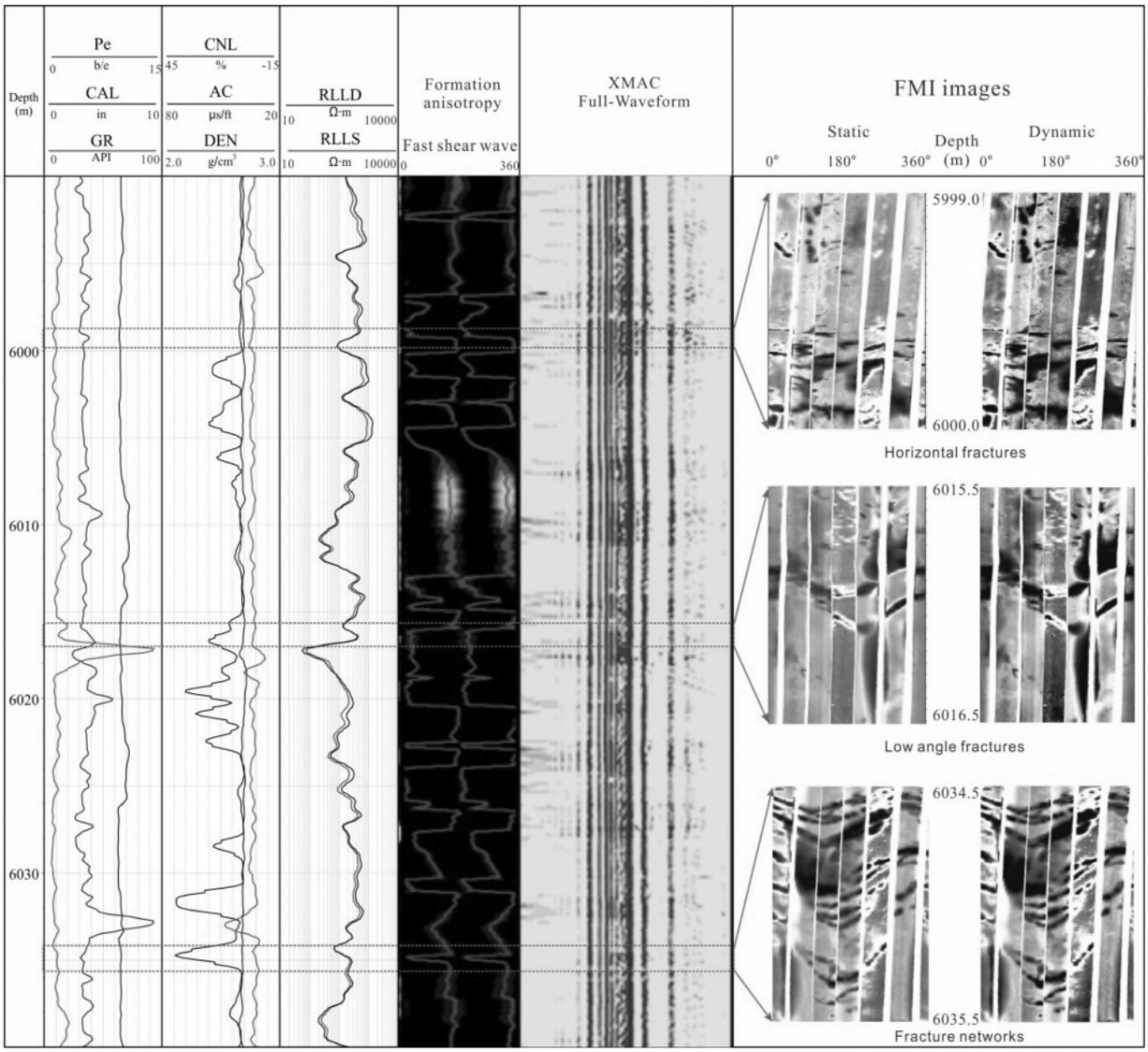

Fig. 12. Well log (conventional, image and XMAC sonic log) expressions of open high angle fractures and fracture network in the Cambrian dolostones in Tarim Basin (Ls2). The presence of open high angle fractures and fracture network will cause attenuation of sonic full-waveform.

observation prove the presences of vuggy fractures (Figs. 7, Fig.10, Fig. 12). Many fractures could act as fluid pathways and facilitate or expedite the dissolution process (Dashti et al., 2018), and the microscopic thin section observations support the existence of enlargement of the pre-existing natural fractures (Fig. 8).

Image logs can be used to directly pick out the fracture attitudes (dip direction, dip angles), and in addition, the fracture parameters such as fracture length (FVTL), fracture porosity (FVPA), and fracture density (FVDC) can be calculated from the image logs in case of water based drilling muds (Prioul and Jocker, 2009; Zeng et al., 2013; Lai et al., 2018). From Fig. 14, it can also be concluded that the fractures are formed in fine crystalline dolostones (white-grey), while there are no fractures in dolomicrite (dark grey). The presences of natural fractures result in a deviation of deep and shallow lateral logs (Fig. 14). When calibrated with the core analysis with the image log and related fracture parameters, it is found that there are dissolution along the fracture surface, and dissolution along the fracture plane increase the fracture porosity (Fig. 14).

The Well Zs 1 (Fig. 1), which was drilled in the Tazhong Uplift (or Central Uplift) in the year 2012 (Fig. 15), revealed the exploration prospect of Cambrian dolostones in Tarim basin (Wang et al., 2018). High hydrocarbon production rate (daily natural gas production of 3×10^4 m^3, and daily water production of 34 m^3) is encountered in the ultra-deep (6597.63–6785.00 m) Cambrian Xiaoerbulake dolostones (Shen et al., 2016; Wang et al., 2018). There are four faults developed in the Cambrian dolostones, which cut through underlying basin basements, and therefore hydrothermal fluids related to the hydrothermal events (Permian magmatic activity) could migrate upward along fault or fracture surfaces (Dong et al., 2013; Jiang et al., 2015). Large faults often have a clear damage zone, which can be evidenced by increase of fractures towards the faults (Peacock, 2001). Deep faults and related fractures are the conduits allowing the hydrothermal fluids to migrate upward due to thermal convections (Zhu et al., 2015b). The upward migrating fluids will dissolve the dolostones, forming secondary fabric

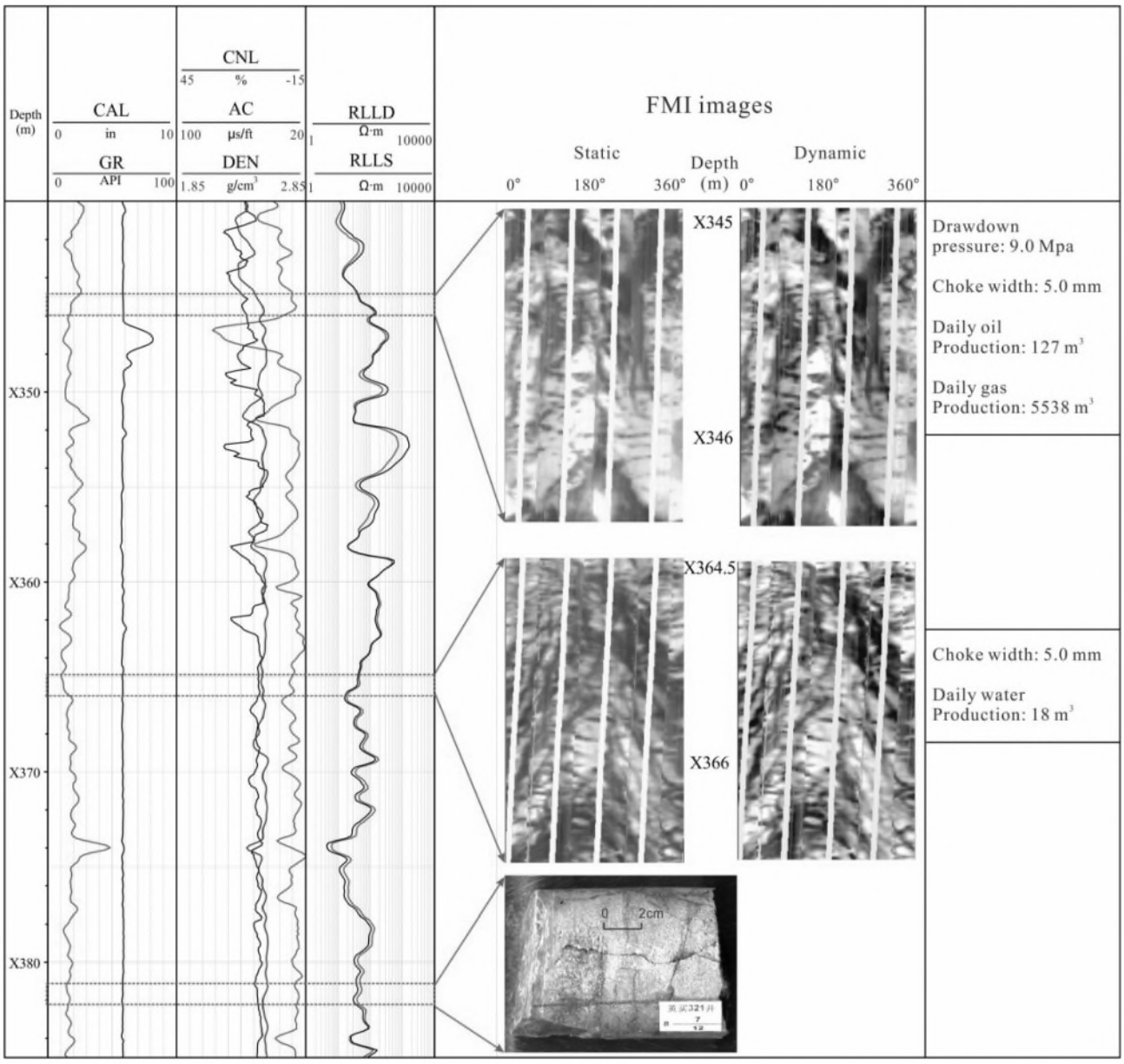

Fig. 13. Fractures and their controls on hydrocarbon productivity (YM 321). The presence of natural fractures will enhance hydrocarbon productivity.

dissolution pores and intercrystal dissolution pores (Zhu et al., 2015a; Li et al., 2016; Jiang et al., 2016, 2018). Additionally, the dolostones adjacent to the main faults will be heavily fractured (Wilson et al., 2007), and the open fractures can act as the migration pathways for hydrothermal fluids, and thus further dissolving the matrix dolostones, forming vuggy fractures (Fig. 15). The dominance of dissolution pores (fabric dissolution pores, intercrystal dissolution and enlarged dissolution pores) and the presence of saddle dolomites in the Cambrian dolostones prove that the Cambrian dolomites had experienced hydrothermal dissolution (Zhang et al., 2009; Zhu et al., 2015b; Guo et al., 2016; Jiang et al., 2016, 2018).

As can be seen from Fig. 15, the dolostones are intensively fractured in the depth intervals from 6799 to 6187 m, which are adjacent to the deep faults, additionally, most of the fractures are vuggy, implying dissolution along the fracture surface had occurred. Conversely, for the depth intervals from 6619 to 6621 m (far away from the deep faults), the fracture intensity become lower, and the dissolution along the fracture surface has not been observed (Fig. 15). Fig. 16 (6735–6790 m depth interval in Well Zs1) also supports that there is an increasing trend for fracturing and related dissolution with the burial depths in Well Zs1. The deep burial intervals (6784–6786 m) are highly fractured, and dissolution along fracture plane is very common, forming vuggy fractures (Fig. 16). With the shallowing burial depths (6765–6768 m) (relatively far away from the deep faults), the dolostones are not very heavily fractured, and fracture intensity becomes much lower at the shallow burial depths, and additionally dissolution along the fracture plane almost disappeared (Fig. 16).

The fracture density (FVDC), fracture porosity (FVPA) and fracture length (FVTL), which can be calculated from image logs, have increasing trends with burial depths (Fig. 16). For instance, the fracture porosity can reach as much as 0.15% where the dolostones are heavily fractured, in addition, the linear fracture density can be as high as 5 numbers per meter (Fig. 16). The decreasing of dual lateral log values (RLLD and RLLS) with increasing burial depths also proves the increasing fracture intensity with the burial depths (Fig. 16). Therefore the dolostones adjacent to the deep faults are easily to be fractured, and the presences of fractures promote the hydrothermal fluids flow, and will further improve reservoir quality by enhancing dissolution (Jiang et al., 2015; Zhu et al., 2015a; Guo et al., 2016).

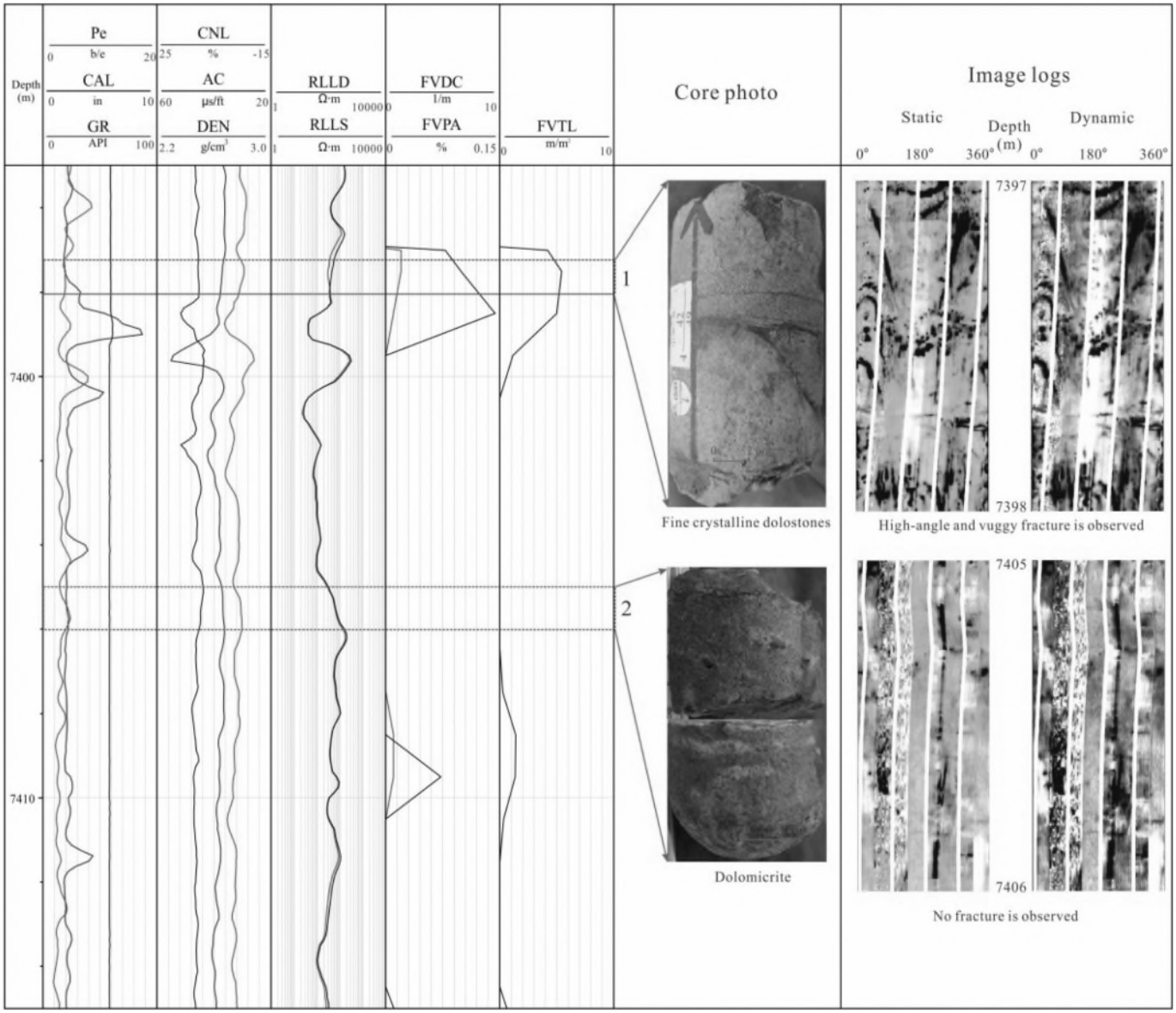

Fig. 14. Fracture evaluated by core, conventional well logs and image logs (Zh 1). Fracture recognized by core observation can also be detected by image logs, and the image log provide fracture density (FVDC), fracture porosity (FVPA), and fracture length (FVTL).

6. Conclusions

(1) Matrix dolomites in Cambiran dolostones of the Tarim Basin include dolomicrite, microbial dolomites, crystalline dolomites, and the dolomite cements include saddle dolomites or crystalline dolomites. The matrix permeability of the Cambiran dolostones is poor, and fractures play an important role in enhancing permeability.

(2) In situ stress field (SH_{max} direction) is determined from image log derived drilling induced fractures, borehole breakouts and sonic log derived shear wave birefringence. Open to partly open to closed natural fractures and with various dip direction and dip angles are recognized in the Cambrian dolostones. Natural fractures are mainly formed in the dolograinstone, and fine-medium-coarse crystalline dolostones, while fractures in the dolomicrites and gypsums-bearing dolostones are rare. The natural fractures are classified into high angle fracture, low-medium dip angle fractures, and low angle or horizontal fractures. Vuggy fractures (dissolution along the fracture plane) and micro-fractures with aperture less than 0.1 mm are detected by core observation and thin section analysis.

(3) The presences of open fractures cause minor deviations on the DEN logs, while resistivity values will be significantly reduced, in addition the sonic transit time (AC) will be significantly increased in front of fractures. The energy of XMAC sonic full-waveforms will be strongly attenuated in front of open fractures. However, the closed to partly closed fractures are recognized as bright to dark continuous sine waves on the image logs, and the natural factures appear as dark sine wave appearances.

(4) Fractures with strike parallel to the SH_{max} direction are suggested to have good connectivity, and significantly enhance hydrocarbon productivity. Deep faults connect the basin basements and underlying dolostones act as migration pathways for fluid flow, and the dolostones adjacent to the faults are heavily fractured. The presences of natural fractures enhance dissolution, forming enlarged dissolution pores and intercrystal dissolution pores.

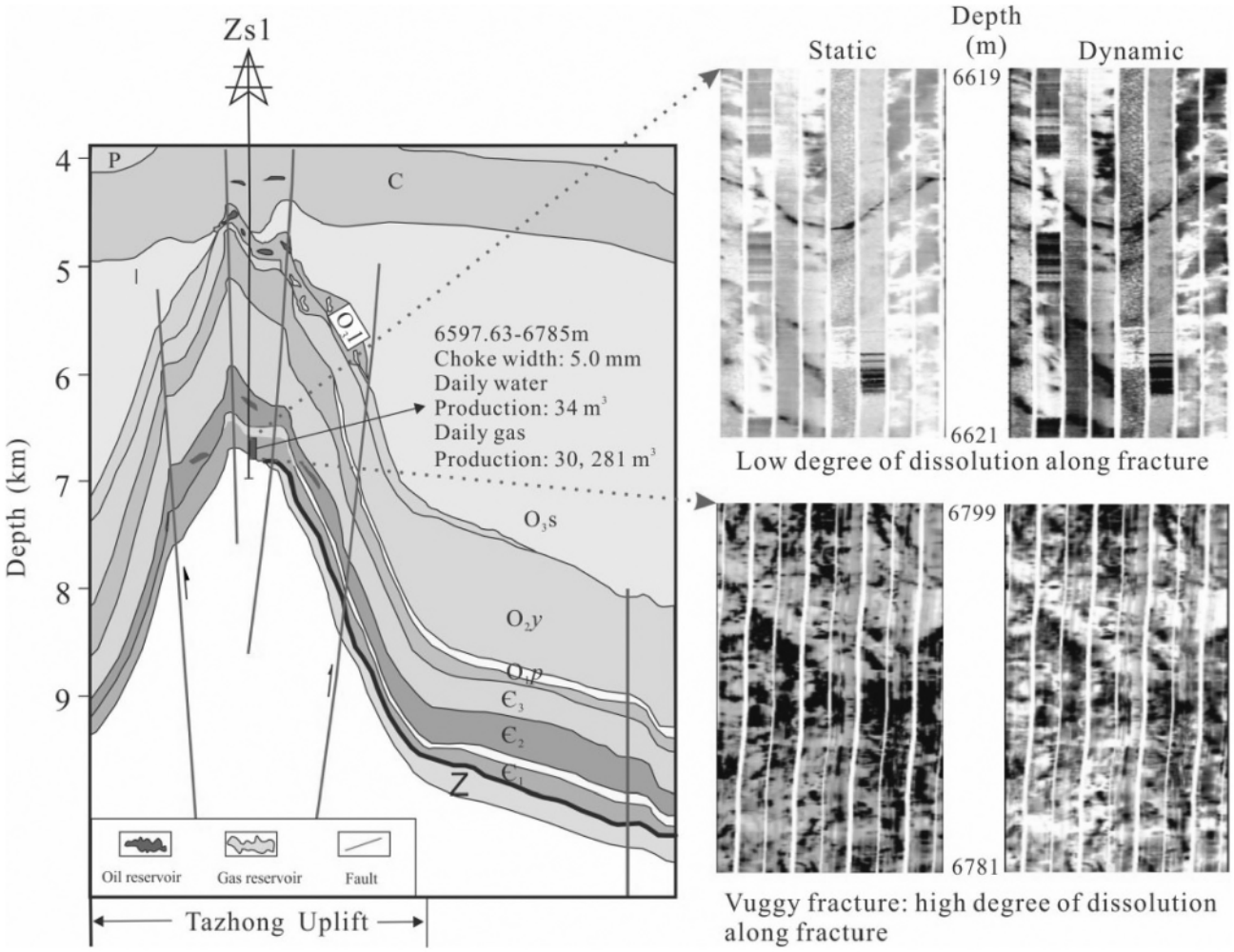

Fig. 15. Cross section of the Tazhong Uplift showing hydrocarbon accumulation for Well Zs 1 (Wang et al., 2018; Zhu et al., 2016). The dolostones adjacent to the faulted zone are heavily fractured, and a high degree of dissolution.

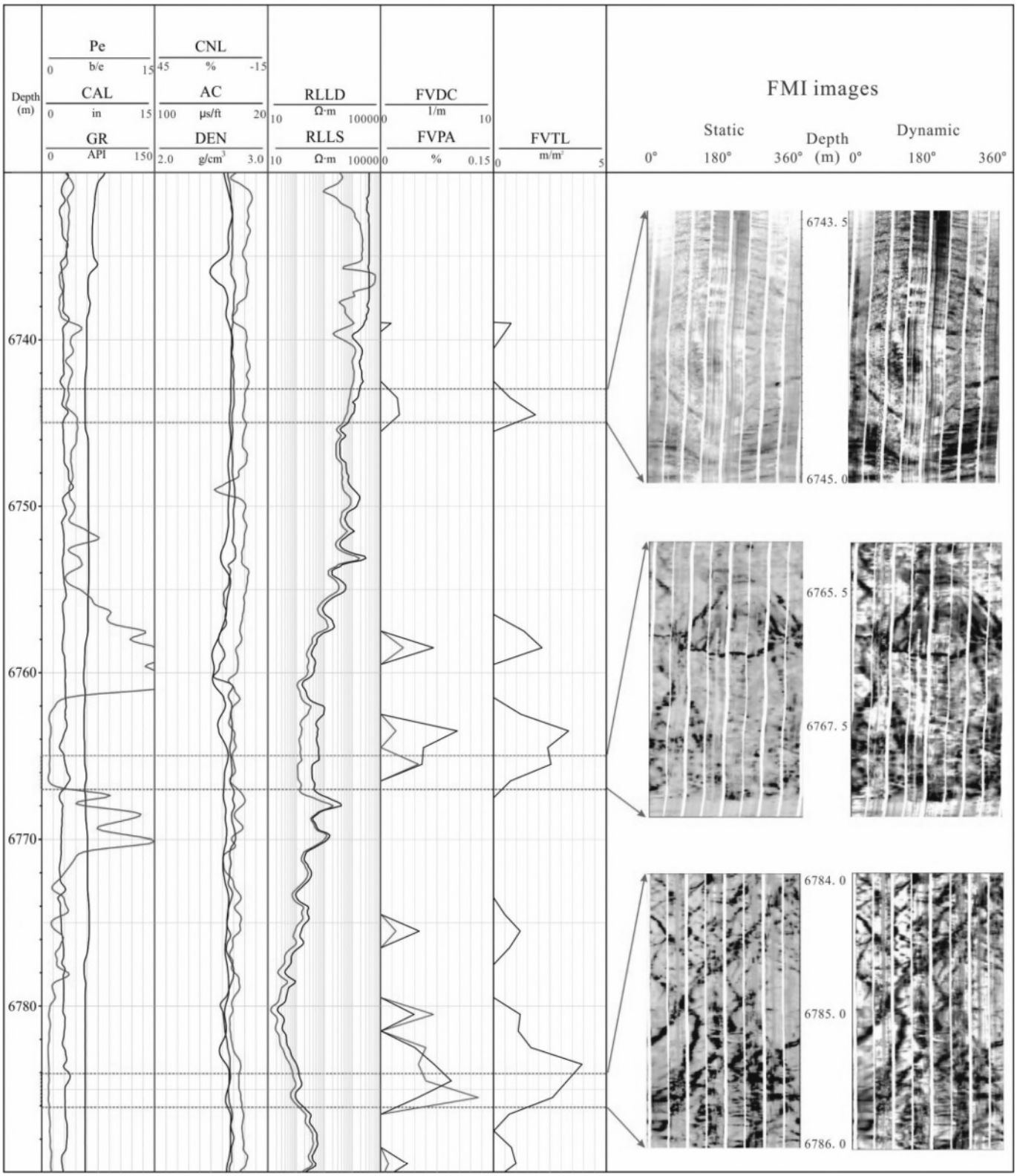

Fig. 16. Effect of fractures on enhancing dissolution (Zs 1). The dolostones, though are deeper buried, are heavily fractures due to adjacent to the faulted zone, and a high degree of dissolution is encountered.

Declaration of competing interest

The authors declare that they have no known competing financialinterestsor personal relationships that could have appeared to influence the work reported in this paper.

CRediT authorship contribution statement

Jin Lai: Conceptualization, Methodology, Software, Data curation, Writing - original draft, Writing - review & editing. **Kangjun Chen:** Conceptualization, Methodology, Software. **Yi Xin:** Data curation, Writing - original draft. **Xingneng Wu:** Data curation, Writing - original draft. **Xu Chen:** Visualization, Investigation. **Kefu Yang:** Visualization, Investigation. **Qiuqiang Song:** Writing - review & editing. **Guiwen Wang:** Software, Validation, Writing - review & editing. **Xiujian Ding:** Writing - review & editing.

Acknowledgments

This work is financially supported by Science Foundation of China University of Petroleum, Beijing (No.2462017YJRC023), the Fundamental Research Funds for the Central Universities and the Opening Fund of Key Laboratory of Deep Oil & Gas (20CX02116A). The authors would like to express their sincere thanks to the PetroChina Tarim Oilfield Company for their assistance in providing the information, and for their technical input to this work. This study is based on work carried out by a large group of participants. We thank the staff of the research institute of petroleum exploration and development of PetroChina Tarim oilfield company. The software Geoframe and Techlog were used to produce the borehole images. We thank Hangzhou Institute of Geology, Research Institute of Petroleum Exploration and Development of PetroChina for their work. We are also grateful to the three reviewers, whose comments improved the quality of this manuscript. We thank Editor of JPSE for his enthusiasm, patience and tireless efforts.

Appendix A. Supplementary data

Supplementary data to this article can be found online at https://doi.org/10.1016/j.petrol.2020.107659.

References

Aghli, G., Soleimani, B., Moussavi-Harami, R., Mohammadian, R., 2016. Fractured zones detection using conventional petrophysical logs by differentiation method and its correlation with image logs. J. Petrol. Sci. Eng. 142, 152–162.

Aghli, G., Moussavi-Harami, R., Mohammadian, R., 2020. Reservoir heterogeneity and fracture parameter determination using electrical image logs and petrophysical data (a case study, carbonate Asmari Formation, Zagros Basin, SW Iran). Petrol. Sci. 17, 51–69.

Aleardi, M., Mazzotti, A., Tognarelli, A., Ciuffi, S., Casini, M., 2015. Seismic and well log characterization of fractures for geothermal exploration in hard rocks. Geophys. J. Int. 203, 270–283.

Ameen, M.S., MacPherson, K., Al-Marhoon, M.I., Rahim, Z., 2012. Diverse fracture properties and their impact on performance in conventional and tight-gas reservoirs, Saudi Arabia: the Unayzah, South Haradh case study. AAPG (Am. Assoc. Pet. Geol.) Bull. 96 (3), 459–492.

Anders, M.H., Laubach, S.E., Scholz, C.H., 2014. Microfractures: a review. J. Struct. Geol. 69 (Part B), 377–394.

Assousa, S., Elkington, P., 2014. Phase-based dispersion analysis for acoustic array borehole logging data. J. Acoust. Soc. Am. 135 (4), 1919–1928.

Bell, J.S., Gough, D.I., 1979. Northeast-southwest compressive stress in alberta evidence from oil wells. Earth Planet Sci. Lett. 45 (2), 475–482.

Brandes, C., Tanner, D., 2020. Fault mechanics and earthquakes. In: Tanner, D., Brandes, C. (Eds.), Understanding Faults. Elsevier, pp. 11–80.

Brekke, H., MacEachern, J.A., Roenitz, T., Dashtgard, S.E., 2017. The use of microresistivity image logs for facies interpretations: an example in point-bar deposits of the McMurray Formation, Alberta, Canada. AAPG (Am. Assoc. Pet. Geol.) Bull. 101 (5), 655–682.

Brudy, M., Zoback, M.D., 1999. Drilling-induced tensile wall-fractures: implications for determination of in situ stress orientation and magnitude. Int. J. Rock Mech. Min. Sci. 36, 191–215.

Chen, J., Xu, Y., Huang, D., 2000. Geochemical characteristics and origin of natural gas in Tarim basin, China. AAPG (Am. Assoc. Pet. Geol.) Bull. 84 (5), 591–606.

Collett, T.S., Lewis, R.E., Winters, W.J., Lee, M.W., Rose, K.K., Boswell, R.M., 2011. Downhole well log and core montages from the mount elbert gas hydrate stratigraphic test well, Alaska north slope. Mar. Petrol. Geol. 28, 561–577.

Crampin, S., 1985. Evaluation of anisotropy by shear-wave splitting. Geophysics 50, 142–152.

Dashti, R., Rahimpour-Bonab, H., Zeinali, M., 2018. Fracture and mechanical stratigraphy in naturally fractured carbonate reservoirs-A case study from Zagros region. Mar. Petrol. Geol. 97, 466–479.

Dong, S., Chen, D., Qing, H., Zhou, X., Wang, D., Guo, Z., Jiang, M., Qian, Y., 2013. Hydrothermal alteration of dolostones in the Lower Ordovician, Tarim Basin, NW China: multiple constraints from petrology, isotope geochemistry and fluid inclusion microthermometry. Mar. Petrol. Geol. 46, 270–286.

Dong, S., Chen, D., Zhou, X., Qian, Y., Tian, M., Qing, H., 2017. Tectonically driven dolomitization of Cambrian to Lower Ordovician carbonates of the Quruqtagh area, north-eastern flank of Tarim Basin, north-west China. Sedimentology 64, 1079–1106.

Du, Y., Fan, T., Machel, H.G., Gao, Z., 2018. Genesis of Upper Cambrian-Lower Ordovician dolomites in the Tahe oilfield, Tarim basin, NW China: several limitations from petrology, geochemistry, and fluid inclusions. Mar. Petrol. Geol. 91, 43–70.

Etchecopar, A., Yamada, T., Cheung, P., 2013. Borehole images for assessing present day stresses. Bull. Soc. Geol. Fr. 184 (4–5), 307–318.

Folkestad, A., Veselovsky, Z., Roberts, P., 2012. Utilising borehole image logs to interpret delta to estuarine system: a case study of the subsurface Lower Jurassic Cook Formation in the Norwegian northern North Sea. Mar. Petrol. Geol. 29, 255–275.

Fu, Q., 2019. Characterization and discrimination of paleokarst breccias and pseudobreccias in carbonate rocks: insight from Ordovician strata in the northern Tarim Basin, China. Sediment. Geol. 382, 61–74.

Gao, Z., Fan, T., 2015. Carbonate platform-margin architecture and its influence on Cambrian-Ordovician reef-shoal development, Tarim Basin, NW China. Mar. Petrol. Geol. 68, 291–306.

Gao, Z., Liu, Z., Gao, S., Ding, Q., Wu, S., Liu, S., 2016. Characteristics and genetic models of Lower Ordovician carbonate reservoirs in southwest Tarim Basin, NW China. J. Petrol. Sci. Eng. 144, 99–112.

Goodall, T.M., Moller, N.K., Ronningsland, T.M., 1998. The integration of electrical image logs 237 with core data for improved sedimentological interpretation. Geological Society. London. Spec. Publ. 136, 237–248.

Guo, C., Chen, D., Qing, H., Dong, S., Li, G., Wang, D., Qian, Y., Liu, C., 2016. Multiple dolomitization and later hydrothermal alteration on the Upper Cambrian-Lower Ordovician carbonates in the northern Tarim basin, China. Mar. Petrol. Geol. 72, 295–316.

Guo, C., Chen, D., Song, Y., Zhou, X., Ding, Y., Zhang, G., 2018. Depositional environments and cyclicity of the early Ordovician carbonate ramp in the western Tarim basin (NW China). J. Asian Earth Sci. 158, 29–48.

Hu, Z., Hu, W., Liu, C., Sun, F., Liu, Y., Li, W., 2019. Conservative behavior of Mg isotopes in massive dolostones: From diagenesis to hydrothermal reworking. Sediment. Geol. 381, 65–75.

Jafari, A., Kadkhodaie-Ilkhchi, A., Sharghi, Y., Ghanavati, K., 2012. Fracture density estimation from perophysical log data using the adaptive neuro-fuzzy inference system. J. Geophys. Eng. 9, 105–114.

Jafari, J., Mahboubi, A., Moussavi-Harami, R., Al-Aasm, I.S., 2020. The effects of diagenesis on the petrophysical and geochemical attributes of the Asmari Formation, Marun oil field, southwest Iran. Petrol. Sci. 17,292–316.

Jiang, L., Pan, W., Cai, C., Jia, L., Pan, L., Wang, T., Li, H., Chen, S., Chen, Y., 2015. Fluid mixing induced by hydrothermal activity in the Ordovician carbonates in Tarim basin, China. Geofluids 15 (3), 483–498.

Jiang, L., Cai, C., Worden, R.H., Crowley, S.F., Jia, L., Zhang, K., Duncan, I.J., 2016. Multiphase dolomitization of deeply buried Cambrian petroleum reservoirs, Tarim Basin, north-west China. Sedimentology 63, 2130–2157.

Jiang, L., Worden, R.H., Cai, C.F., Shen, A., Crowley, S.F., 2018. Diagenesis of an evaporite-related carbonate reservoir in deeply buried Cambrian strata, Tarim basin, Northwest China. AAPG (Am. Assoc. Pet. Geol.) Bull. 102 (1), 77–102.

Ju, W., Shen, J., Qin, Y., Meng, S., Wu, C., Shen, Y., Yang, Z., Li, G., Li, C., 2017. In-situ stress state in the Linxing region, eastern Ordos basin, China: implications for unconventional gas exploration and production. Mar. Petrol. Geol. 86, 66–78.

Keeton, G., Pranter, M., Cole, R.D., Gustason, E.R., 2015. Stratigraphic architecture of fluvial deposits from borehole images, spectral-gamma-ray response, and outcrop analogs, Piceance Basin, Colorado. AAPG (Am. Assoc. Pet. Geol.) Bull. 99 (10), 1929–1956.

Khoshbakht, F., Memarian, H., Mohammadnia, M., 2009. Comparison of Asmari, Pabdeh and Gurpi formation's fractures, derived from image log. J. Petrol. Sci. Eng. 67, 65–74.

Lai, J., Pang, X., Xiao, Q., Shi, Y., Zhang, H., Zhao, T., Chen, J., Wang, G., Qin, Z., 2019b. Prediction of reservoir quality in carbonates via porosity spectrum from image logs. J. Petrol. Sci. Eng. 173, 197–208.

Lai, J., Wang, G., Chai, Y., Xin, Y., Wu, Q., Zhang, X., Sun, Y., 2017a. Deep burial diagenesis and reservoir quality evolution of high-temperature, high-pressure sandstones: examples from Lower Cretaceous Bashijiqike Formation in Keshen area, Kuqa depression, Tarim basin of China. AAPG (Am. Assoc. Pet. Geol.) Bull. 101 (6), 829–862.

Lai, J., Wang, G., Fan, Z., Wang, Z., Chen, J., Zhou, Z., Wang, S., Xiao, C., 2017b. Fracture detection in oil-based drilling mud using a combination of borehole image and sonic logs. Mar. Petrol. Geol. 84, 195–214.

Lai, J, Wang, G, Fan, Z, Chen, J, Qin, Z, Xiao, C, Wang, S, Fan, X, 2017d. Three-dimensional quantitative fracture analysis of tight gas sandstones using industrial computed tomography. Sci. Rep. 7 (1), 18–25.

Lai, J., Wang, G., Fan, Z., Chen, J., Wang, S., Fan, X., 2017c. Sedimentary characterization of a braided delta using well logs: the Upper Triassic Xujiahe formation in central Sichuan basin, China. J. Petrol. Sci. Eng. 154, 172–193.
Lai, J., Wang, G., Wang, S., Cao, J., Li, M., Pang, X., Han, C., Fan, X., Yang, L., He, Z., Qin, Z., 2018. A review on the applications of image logs in structural analysis and sedimentary characterization. Mar. Petrol. Geol. 95, 139–166.
Lai, J., Li, D., Wang, G., Xiao, C., Hao, X., Luo, Q., Lai, L., Qin, Z., 2019a. Earth stress and reservoir quality evaluation in high and steep structure: the Lower Cretaceous in the Kuqa Depression, Tarim Basin, China. Mar. Petrol. Geol. 101, 43–54.
Lai, J., Wang, S., Wang, G., Shi, Y., Zhao, T., Pang, X., Fan, X., Qin, Z, Fan, X., 2019c. Pore structure and fractal characteristics of Ordovician Majiagou carbonate reservoirs in Ordos basin, China. AAPG Bull. 103 (11), 2573–2596.
Lai, J., Wang, S., Zhang, C., Wang, G., Song, Q., Chen, X., Yang, K., Yuan, C., 2020. Spectrum of pore types and networks in the deep cambrian to lower ordovician dolostones in Tarim basin, China. Mar. Petrol. Geol. 112, 104081.
Li, H., Cai, C., 2017. Origin and evolution of formation water from the Ordovician carbonate reservoir in the Tazhong area, Tarim basin, NW China. J. Petrol. Sci. Eng. 148, 103–114.
Li, Q., Jiang, Z., Hu, W., You, X., Hao, G., Zhang, J., Wang, X., 2016. Origin of dolomites in the Lower Cambrian Xiaoerbulak formation in the Tarim basin, NW China: implications for porosity development. J. Asian Earth Sci. 115, 557–570.
Liu, J., Ding, W., Yang, H., Wang, R., Yin, S., Li, A., Fu, F., 2017. 3D geomechanical modeling and numerical simulation of in-situ stress fields in shale reservoirs: a case study of the lower Cambrian Niutitang formation in the Cen'gong block, South China. Tectonophysics 712–713, 663–683.
Liu, J., Ding, W., Wang, R., Yang, H., Wang, X., Li, A., 2018. Correlation analysis of element contents and mechanical characteristics of shale reservoirs: a case study in the Cen'gong block, South China. Mar. Petrol. Geol. 91, 19–28.
Lu, X., Wang, Y., Tian, F., Li, X., Yang, D., Li, T., Lv, Y., He, X., 2017. New insights into the carbonate karstic fault system and reservoir formation in the southern Tahe area of the Tarim basin. Mar. Petrol. Geol. 86, 587–605.
Luczaj, J.A., Harrison, W.B., Williams, N.S., 2006. Fractured hydrothermal dolomite reservoirs in the devonian dundee formation of the central Michigan basin. AAPG (Am. Assoc. Pet. Geol.) Bull. 90 (11), 1787–1801.
Lynn, H.B., 2016. Image-log calibration of fracture-azimuth and fracture-density attributes from OVT prestack depth-migrated data. Lead. Edge 35 (2), 164–169.
Lyu, W., Zeng, L., Liu, Z., Liu, G., Zu, K., 2016. Fracture responses of conventional logs in tight-oil sandstones: a case study of the Upper Triassic Yanchang Formation in southwest Ordos Basin, China. AAPG (Am. Assoc. Pet. Geol.) Bull. 100 (9), 1399–1417.
Nelson, R.A., 2001. Geologic Analysis of Naturally Fractured Reservoirs, second ed. Gulf Professional Publishing, Woburn, Massachusetts, p. 332.
Nian, T., Wang, G., Xiao, C., Zhou, L., Deng, L., Li, R., 2016. The in situ stress determination from borehole image logs in the Kuqa Depression. J. Nat. Gas Sci. Eng. 34, 1077–1084.
Nian, T., Wang, G., Song, H., 2017. Open tensile fractures at depth in anticlines: a case study in the Tarim basin, NW China. Terra. Nova 29 (3), 183–190.
Ngia, N.R., Hu, M., Gao, D., 2019. Tectonic and geothermal controls on dolomitization and dolomitizing fluid flows in the Cambrian-Lower Ordovician carbonate successions in the western and central Tarim Basin, NW China. J. Asian Earth Sci. 172, 359–382.
Nian, T., Jiang, Z., Wang, G., Xiao, C., He, W., Fei, L., He, Z., 2018. Characterization of braided river-delta facies in the Tarim Basin Lower Cretaceous: application of borehole image logs with comparative outcrops and cores. Mar. Petrol. Geol. 97, 1–23.
Nie, X., Zou, C., Pan, L., Huang, Z., Liu, D., 2013. Fracture analysis and determination of in-situ stress direction from resistivity and acoustic image logs and core data in the Wenchuan Earthquake Fault Scientific Drilling Borehole-2 (50–1370 m). Tectonophysics 593, 161–171.
Niu, H., Liu, S., Lai, J., Wang, G., Liu, B., Xie, Y., Xie, W., 2020. In-situ stress determination and fracture characterization using image logs. Energy Sci. Eng. 8, 476–489.
Olson, J.E., Laubach, S.E., Lander, R.H., 2009. Natural fracture characterization in tight-gas sandstones: integrating mechanics and diagenesis. AAPG (Am. Assoc. Pet. Geol.) Bull. 93, 1535–1549.
Peacock, D.C.P., 2001. The temporal relationship between joints and faults. J. Struct. Geol. 23, 329–341.
Peacock, D.C.P., Nixon, C.W., Rotevatn, A., Sanderson, D.J., Zuluaga, L.F., 2016. Glossary of fault and other fracture networks. J. Struct. Geol. 92, 12–29.
Prioul, R., Jocker, J., 2009. Fracture characterization at multiple scales using borehole images, sonic logs, and walkaround vertical seismic profile. AAPG (Am. Assoc. Pet. Geol.) Bull. 93 (11), 1503–1516.
Prioul, R., Donald, A., Koepsell, R., Marzouki, Z.E., Bratton, T., 2007. Forward modeling of fracture-induced sonic anisotropy using a combination of borehole image and sonic logs. Geophysics 72 (4), 135–147.
Qiu, N.S., Chang, J., Zuo, Y.H., Wang, J.Y., Li, H.L., 2012. Thermal evolution and maturation of lower Paleozoic source rocks in the Tarim Basin, northwest China. AAPG (Am. Assoc. Pet. Geol.) Bull. 96 (5), 789–821.
Schlumberger, 2004. Schlumberger WTA Marketing Service: FMI Fullbore Formation MicroImager. Schlumberger Educational Services, Houston, Texas, p. 2.
Shazly, T.F., Tarabees, E., 2013. Using of dual laterolog to detect fracture parameters for nubia sandstone formation in rudeis-sidri area, gulf of suez, Egypt. Egypt. J. Petrol. 22, 313–319.
Shen, A.J., Zheng, J.F., Chen, Y.Q., Ni, X.F., Huang, L.L., 2016. Characteristics, origin and distribution of dolomite reservoirs in lower-middle cambrian, Tarim basin, NW China. Petrol. Explor. Dev. 43, 375–385.
Su, J., Zhang, S., Huang, H., Wang, Y., Wang, H., He, K., Wang, X., Zhang, B., Wang, H., 2016. New insights into the formation mechanism of high hydrogen sulfide–bearing gas condensates: case study of Lower Ordovician dolomite reservoirs in the Tazhong uplift, Tarim Basin. AAPG (Am. Assoc. Pet. Geol.) Bull. 100 (6), 893–916.
Tian, F., Wang, W., Liu, N., Jiang, J., Niu, C., Zhang, Y., Li, Y., 2018. Rock-type definition and pore characterization of tight carbonate rocks based on thin sections and MICP and NMR experiments. Appl. Magn. Reson. 49 (7), 631–652.
Tian, F., Luo, X., Zhang, W., 2019. Integrated geological-geophysical characterizations of deeply buried fractured-vuggy carbonate reservoirs in Ordovician strata, Tarim Basin. Mar. Petrol. Geol. 99, 292–309.
Wang, Guiwen, Jin, Lai, Bingchang, Liu, Fan, Zhuoying, Liu, Shichen, Shi, Yujiang, Zhang, Haitao, 2020. Fluid property discrimination in dolostone reservoirs using well logs. Acta Geologica Sinica (English Edition) 94 (3), 831–846.
Wang, S., Cao, Y., Du, D., Wang, S., Li, H., Dong, H., Yan, W., Bai, Y., 2018. The characteristics and main controlling factors of dolostone reservoir in Lower Cambrian Xiaoerbulak Formation in Keping-Bachu area, Tarim Basin, NW China. Natl. Gas Geosci. 29 (6), 784–795.
Warren, J., 2000. Dolomite: occurrence, evolution and economically important associations. Earth Sci. Rev. 52, 1–81.
Wilson, M.E.J., Evans, M.J., Oxtoby, N.H., Nas, D.S., Donnelly, T., Thirlwall, M., 2007. Reservoir quality, textural evolution, and origin of fault-associated dolomites. AAPG (Am. Assoc. Pet. Geol.) Bull. 91 (9), 1247–1272.
Wilson, T.H., Smith, V., Brown, A., 2015. Developing a model discrete fracture network, drilling, and enhanced oil recovery strategy in an unconventional naturally fractured reservoir using integrated field, image log, and three-dimensional seismic data. AAPG Bull. 99 (4), 735–762.
Xu, J., Zhang, B., Qin, Y., Cao, G., Zhang, H., 2016. Method for calculating the fracture porosity of tight-fracture reservoirs. Geophysics 81 (4), IM57–IM70.
Zaree, V., Riahi, M.A., Khoshbakht, F., Hemmati, H.R., 2016. Estimating fracture intensity in hydrocarbon reservoir: an approach using DSI data analysis. Carbonates Evaporites 31, 101–107.
Zazoun, R.S., 2013. Fracture density estimation from core and conventional well logs data using artificial neural networks: the Cambro-Ordovician reservoir of Mesdar oil field, Algeria. J. Afr. Earth Sci. 83, 55–73.
Zeng, L., 2010. Microfracturing in the upper triassic sichuan basin tight-gas sandstones: tectonic, overpressure, and diagenetic origins. AAPG (Am. Assoc. Pet. Geol.) Bull. 94 (12), 1811–1825.
Zeng, L.B., Li, X.Y., 2009. Fractures in sandstone reservoirs with ultra-low permeability: a case study of the upper triassic yanchang formation in the ordos basin, China. AAPG (Am. Assoc. Pet. Geol.) Bull. 93 (4), 461–477.
Zeng, L., Su, H., Tang, X., Peng, Y., Gong, L., 2013. Fractured tight sandstone oil and gas reservoirs: a new play type in the Dongpu depression, Bohai Bay Basin, China. AAPG (Am. Assoc. Pet. Geol.) Bull. 97 (3), 363–377.
Zhang, J., Hu, W., Qian, Y., Wang, X., Cao, J., Zhu, J., Li, Q., Xie, X., 2009. Formation of saddle dolomites in Upper Cambrian carbonates, western Tarim basin (northwest China): implications for fault-related fluid flow. Mar. Petrol. Geol. 26, 1428–1440.
Zhao, W.Z., Shen, A.J., Hu, S.Y., Pan, W.Q., Zheng, J.F, Qiao, Z.F., 2012. Types and distributional features of Cambrian-Ordovician dolostone reservoirs in Tarim Basin, northwestern China. Acta Petrol. Sin. 28 (3), 758–768.
Zhao, W.Z., Shen, A.J., Zhou, J.G., Wang, X.F., Lu, J.M., 2014. Types, characteristics, origin and exploration significance of reef-shoal reservoirs: a case study of Tarim Basin, NW China and Sichuan Basin, SW China. Petrol. Explor. Dev. 41, 283–293.
Zhao, J., Tang, D., Qin, Y., Xu, H., 2018. Experimental study on structural models of coal macrolithotypes and its well logging responses in the Hancheng area, Ordos Basin, China. J. Petrol. Sci. Eng. 166, 658–672.
Zhu, D., Meng, Q., Jin, Z., Hu, W., 2015a. Fluid environment for preservation of pore spaces in a deep dolomite reservoir. Geofluids 15, 527–545.
Zhu, D., Meng, Q., Jin, Z., Liu, Q., Hu, W., 2015b. Formation mechanism of deep Cambrian dolomite reservoirs in the Tarim basin, northwestern China. Mar. Petrol. Geol. 59, 232–244.
Zhu, G., Wang, H., Weng, N., 2016. TSR-altered oil with high-abundance thiaadamantanes of a deepburied Cambrian gas condensate reservoir in Tarim Basin. Mar. Petrol. Geol. 69, 1–12.